aerospace

MDPI

Article

Effect of Solid-to-Gas Ratio on Powder Fuel Mixing in a Cavity-Based Supersonic Combustion Chamber with Induced Shock: A Numerical Study

Zuodong Liang, Ming Jiang, Shaoqing Hu, Kai Ma, Guiyang Xu, Wenjie Wang, Yuezu Miao and Hongyan Li *

Xi'an Modern Chemistry Research Institute, Xi'an 710065, China
* Correspondence: chipsme@126.com

Abstract: The development of powder-fueled ramjets is challenged by the mechanisms of flow mixing for the combustion of powder fuel in supersonic airflows. This paper describes a series of numerical simulations on the injection process of boron powder fuel in a cavity-based supersonic combustion chamber with induced shock. Under different solid-to-gas ratios ranging from 20 to 0.1, this study explored the evolution of supersonic flow fields with strong shear and discontinuities. It also discusses the flow processes and mixing characteristics of powder fuel within them. The study found that the enhancement of powder fuel mixing is mainly related to the rotational regions of large-scale vortex structures. Vortex structures with the required intensity and area can be obtained by adjusting the appropriate solid-to-gas ratio. Moreover, reasonable induction methods can enhance the interaction between particles and vortex structures, thereby achieving mixing enhancement. The interaction between powder fuels and the peripheral rotating regions of these vortices significantly improves the mixing efficiency, with the highest average mixing efficiency increased by 30%. This research lays a foundation for developing mixing enhancement strategies and supports the advancement of efficient and stable powder-fueled ramjets.

Keywords: powder-fueled ramjet; powder fuel; multiphase flows; particle flows; mixing characteristics; shock wave

Academic Editor: James 'Chris' Thomas

Received: 26 November 2024
Revised: 14 January 2025
Accepted: 16 January 2025
Published: 19 January 2025

Citation: Liang, Z.; Jiang, M.; Hu, S.; Ma, K.; Xu, G.; Wang, W.; Miao, Y.; Li, H. Effect of Solid-to-Gas Ratio on Powder Fuel Mixing in a Cavity-Based Supersonic Combustion Chamber with Induced Shock: A Numerical Study. *Aerospace* **2025**, *12*, 70. https://doi.org/10.3390/aerospace12010070

1. Introduction

Ramjets, which stand out as one of the most effective propulsion systems for achieving and sustaining supersonic flight, play a crucial role in the development of advanced supersonic flights [1]. Traditionally fueled by liquid or solid rocket fuels, ramjets have seen the introduction of forms like powder and gel fuels. The concept of powder-fueled ramjets first emerged in the late 1940s to counteract thrust reduction issues in supersonic conditions caused by the pyrolysis of hydrocarbon fuels [2,3]. Initial experiments by the Glenn Research Center demonstrated the feasibility of using aluminum powder as fuel [4]. However, challenges like nozzle clogging by metal oxides and technological limitations hampered progress [5].

In 2001, Goroshin re-evaluated the viability of metal powder fuels, highlighting their advantages in specific impulse and storage conditions, though modifications like pre-burners were necessary [6]. This rekindled interest in powder-fueled ramjets, which offer high specific impulse, low storage requirements, and amphibious potential if challenges are addressed [7,8]. Research over the following years focused on the combustion characteristics of various metal powders, including Mg, Al, Zr, B [9,10], Ti [11], and Ni [12], with sizes

ranging from micrometers to nanometers. Subsequent research by the National University of Defense Technology [13] and Northwestern Polytechnical University [14] demonstrated the feasibility of powder-fueled ramjets through ground-based tests, achieving significant combustion efficiency and operational reliability [15]. These studies also effectively confirmed working characteristics such as repeated start and stop [16]. A remarkable test achieved 24 s of self-sustaining combustion with a 73.05% efficiency using Al powder fuel [17]. With the advances and rekindled interest in powder fuels, researchers began to notice the complexity of the combustion process. Researchers found that the combustion process of powder particles is much more complex than that of liquid or gaseous fuels [18,19]. This complexity makes achieving stable combustion of particles in supersonic airflow more challenging. Moreover, the metal particles currently used can rarely liquefy and gasify, and their density is much higher than that of liquids or gases. Consequently, solid powder particles have higher inertia and are less likely to change their state of motion. The flow mixing characteristics of powder fuel in a supersonic combustion chamber differ significantly [20]. Therefore, studying the flow and mixing characteristics of powder fuel in such chambers is particularly necessary.

It is essential to note the similarities in mixing mechanisms between gaseous/liquid fuels and powder fuels to address the challenges of mixing powder fuels. Various mixing enhancement techniques have been proposed and implemented in supersonic combustors for gaseous and liquid fuels. Effective fuel mixing is essential for ramjets' stability and thermal cycle efficiency using gaseous fuels, liquid fuels, and other fuels like powder fuel [21,22]. Ben-Yakar et al. used Schlieren visualization and OH planar laser-induced fluorescence to find that ethylene jets penetrate deeper and mix better than hydrogen jets in supersonic crossflow due to large-scale coherent structures [23]. Mai et al. found that introducing an incident shock wave downstream of the injection slot significantly enhances mixing and is crucial for robust flame-holding by creating large-scale recirculation flows [24]. Rana et al. used large eddy simulations to show that Kelvin–Helmholtz instabilities in the upper jet shear layer are crucial for mixing in supersonic crossflow [25]. Sun et al. found that counter-rotating vortex pairs (CVPs) and herringbone separation bubbles enhance fuel mixing in Mach 2.7 supersonic crossflows, with higher momentum flux ratios improving mixing efficiency by forming near-field eddies and primary and secondary trailing counter-rotating vortex pairs (TCVPs) using direct numerical simulations [26,27].

To bridge the understanding of these mechanisms with practical applications, various specific methods have been developed to enhance fuel mixing in supersonic combustors. For instance, wall-mounted transverse jets, induced shock waves, and cavities have proven effective in enhancing mixing. Techer et al. [28] and Sun et al. [26,29] demonstrated that wall-mounted single-hole transverse jets create complex structures that enhance mixing efficiency, with Sun et al.'s simulations showing that Mach disk-induced vortices improve downstream mixing [27]. Liang et al. used nano-tracer-based planar laser scattering (NPLS) and oil flow techniques to highlight the significant effects of bow shocks, barrel shocks, and separation zones on mixing efficiency [30]. Induced shock waves were examined by Mai et al. and Huang et al., who found that incident shocks enhance mixing and flame-holding by creating large-scale recirculation flows and that the shape of shock generators significantly impacts transverse jet flow [24,31]. Gerdroodbary et al.'s simulations further emphasized the importance of shock positions and strengths in mixing efficiency [32]. Regarding cavities, Ukai et al. found that increasing the jet-to-main flow pressure ratio and optimal injection hole positioning enhances mixing within cavities [33,34]. Roos et al. revealed that upstream cavities reduce airflow speed and pressure loss, thereby boosting mixing efficiency [35]. Gruber et al. noted that rearward expansions significantly affect wave structures and fuel entrainment [36]. Yang et al. found that rearward expansions

weaken shock strength, reduce resistance, and minimally impact fuel transport [37]. These techniques enhance mixing by introducing shear layers, complex wave systems, and increasing flow instability. Their effectiveness for gaseous or liquid fuel has been validated through the mentioned experiments and numerical simulations. However, the research on the efficacy of these methods on powder fuel is not yet comprehensive.

Recent studies on powder fuel's flow and mixing process have predominantly utilized numerical simulations as the primary research method. Ding et al. studied the flow characteristics of hydrogen–aluminum two-phase fuel in supersonic inflow. They found that the mixing efficiency of hydrogen is significantly higher than that of aluminum powder under the same conditions. The mixing efficiency of aluminum powder increases with higher injection momentum and inflow Mach number [38]. Additionally, Ding et al. investigated particles with different sizes and densities, finding that as particle size and density increase, so do the velocity and penetration depth of the particles [39,40]. Feng et al. conducted a series of numerical simulations using a cavity-based combustion chamber. The results showed that both particle size and induced shock wave angle affect the flow and mixing of particles [41,42]. Increasing the intensity of the induced shock wave can effectively improve local mixing efficiency [43]. Previous studies have shown that strong shear layers, induced shock waves, and complex wave structures significantly influence the mixing process of powder fuel within combustion chambers. For powder fuels, the supply process requires the addition of fluidizing gas, typically characterized by the solid-to-gas ratio, representing the relationship between fuel's mass flow rates and fluidizing gas. With a constant mass flow rate of powdered fuel, different solid-to-gas ratios necessitate different fluidizing gas flow rates. This difference in solid-to-gas ratios inevitably alters the shock wave structures within the combustion chamber, subsequently affecting the mixing process of powdered fuel in a supersonic combustion chamber.

Given the above analysis, while some research has explored the flow mixing characteristics of powder fuel in a supersonic combustion chamber, it remains limited. The impacts of different solid-to-gas ratios on the mixing characteristics within a combustion chamber featuring both cavity structures and induced shock waves remain unclear. In this paper, the Euler–Lagrangian method is employed to study low flow rates and small particle sizes. It investigates the flow characteristics under different jet solid-to-gas ratios in a cavity-based combustion chamber with induced shock waves. By analyzing the impact of different solid-to-gas ratios on wave structures, vortex structures, particle distribution, and fuel mixing characteristics, this study aims to explore the intrinsic mechanisms influenced by solid-to-gas ratios and their relationship with enhanced supersonic mixing of powder fuel, thereby providing adequate support for achieving stable and self-sustaining combustion in powder-fueled ramjets.

2. Physical Model and Flow Conditions

In this study, a cavity-based combustion chamber is demonstrated in Figure 1. Parts of the structure of this configuration are referenced from the work of Feng et al. [41,43]. The entrance of the combustion chamber has a height of 30 mm and a width of 30 mm. The total length of the combustion chamber is 240 mm. The cavity depth is 12 mm, with a length-to-depth ratio of 7.5. The trailing edge of the cavity is set at an angle of 45°. A single injector is located on the symmetry plane, 10 mm before the cavity. The diameter of the injector is 3.0 mm. This study simplifies the injector structures into a constant-diameter tube with a length of 6.0 mm. The top wall of the chamber features a ramp that induces an induced shock wave. In this study, a 24° ramp generates a shock wave at 50° to the horizontal.

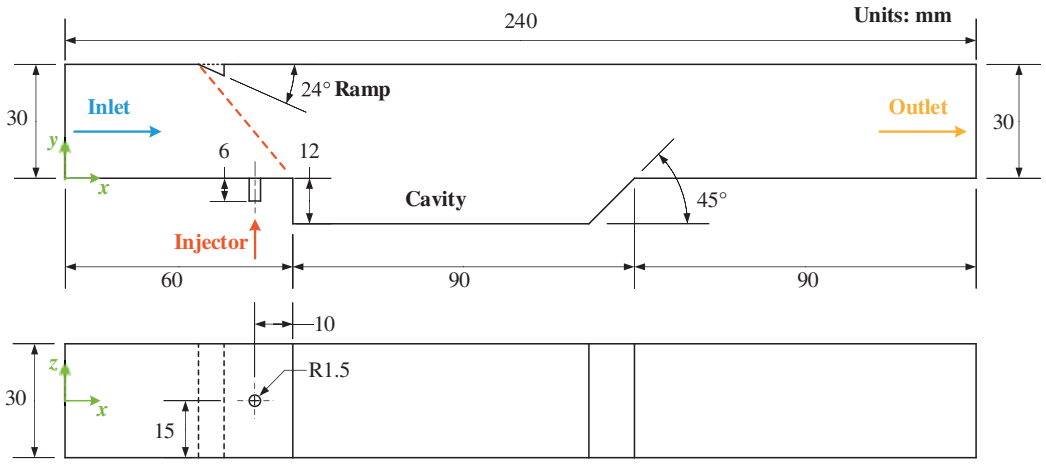

Figure 1. Schematic of the cavity-based supersonic combustion chamber: the top is the front view, and the bottom is the bottom view.

The parameters of supersonic inflow are shown in Table 1. The Mach number of the supersonic inflow is 2.40, while the total pressure and total temperature are 600 kPa and 1200 K, respectively. The inflow gas is air, simplified here to a gaseous mixture consisting of 76.7% N_2 and 23.3% O_2 by mass fraction.

Table 1. Parameters of supersonic inflow.

Gas Type	Mach Number	P_0 (kPa)	T_0 (K)	Velocity (m/s)
Air	2.4	600	1200	1136

The injected fuel type and its density, diameter, and temperature are shown in Table 2. Boron is commonly used as a high-energy metal powder propellant. Numerous studies have been conducted on incorporating boron into conventional hydrocarbon propellants to improve their performance. Among the elements typically utilized in metal powder fuels, the volume calorific value of boron might be the highest at 135.51 MJ/dm^3 [17]. This volume calorific value means that the theoretical release energy of boron in a finite-volume state is much higher than that of conventional hydrocarbon fuels and other common metal powder fuels such as Al and Mg [6]. Furthermore, boron exhibits relatively low biotoxicity. Therefore, it can be argued that boron is the top choice for a metal powder propellant.

Table 2. Parameters of powder fuel.

Fuel Type	$\dot{m}_p$ (g/s)	ρ_p (kg/m^3)	d_p (μm)	T_p (K)
Boron	1.0	2340	5	300

This study selects boron powder with a particle size of 5 μm as the powder fuel. The mass flow rate of powder fuel is 1.0 g/s. The jet gas is nitrogen (N_2), one of the most commonly used gases in powder fuel supply systems [44]. To explore the particle flow characteristics under injection fluid with different solid-to-gas ratio conditions, the solid-to-gas ratio ζ, defined as $\zeta = \dot{m}_p/\dot{m}_g$, is the main focus of this paper. $\dot{m}_p$ is the mass flow rate of powder fuel at the injector inlet, while $\dot{m}_g$ is the mass flow rate of jet gas there. As the particle flow rate $\dot{m}_p$ is constant, different jet mass flow rates $\dot{m}_g$ are achieved by adjusting the total pressure of the jet. The total temperature of the jet is set to 300 K. In this study, the solid-to-gas ratios (ζ) range from 20 to 0.1, corresponding to jet mass flow rates ranging from 0.05 to 10.0 g/s. The specific cases can be found in Table 3.

Table 3. Research conditions.

Case	1	2	3	4	5	6	7	8
Solid-to-gas ratio ζ	20	10	5	2	1	0.5	0.2	0.1
$\dot{m}_g$, g/s	0.05	0.1	0.2	0.5	1.0	2.0	5.0	10.0

3. Numerical Model and Method

In this study, numerical simulation of the injection process of gas–solid two-phase flow was conducted using methods based on the Euler–Lagrangian reference frame. The gas (continuous phase) is solved in the Euler reference frame with the steady method, while the particle (dispersed phase) is solved and tracked in the Lagrangian reference frame with the unsteady method. Mass, momentum, and energy are exchanged between the two phases through source terms. The two-way coupling method is used to solve the gas–particle interaction. The numerical simulations in this study were performed using a platform based on ANSYS FLUENT 2022 R1 kernel.

3.1. Governing Equations of Continuity Phase

The governing equation used in this study for the continuous phase is the compressible Navier–Stokes equation. The equations are as follows [45].

The mass conservation equation is

$$\frac{\partial \rho_g}{\partial t} + \nabla \cdot (\rho_g \vec{v_g}) = S_m \tag{1}$$

The momentum conservation equation is

$$\frac{\partial}{\partial t}(\rho_g \vec{v_g}) + \nabla \cdot (\rho_g \vec{v_g} \vec{v_g}) = -\nabla p_g + \nabla \cdot (\overline{\overline{\tau}}) + \rho_g \vec{g} + S_u \tag{2}$$

The energy equation is

$$\frac{\partial}{\partial t}\left(\rho_g\left(e + \frac{\vec{v_g}^2}{2}\right)\right) + \nabla \cdot \left(\rho \vec{v_g}\left(h + \frac{\vec{v_g}^2}{2}\right)\right) = \nabla \cdot \left(k_{eff}\nabla T - \sum_j h_j \vec{J_j} + \overline{\overline{\tau}} \cdot \vec{v}\right) + S_h \tag{3}$$

ρ_g is the density of the continuous phase, while $\vec{v}_g$ and p_g are the velocity and pressure of the continuous phase. k_{eff} is the effective conductivity, which is the sum of the molecular conductivity k_m and the turbulent thermal conductivity k_t. The source terms S_m, S_u, and S_h represent the mass, momentum, and energy added to the continuous phase from the dispersed phase, respectively. The source terms at the node are calculated with Equations (17) and (18) based on interphase exchange terms of the particles. $\overline{\overline{\tau}}$ is the stress tensor, and it can be given by

$$\overline{\overline{\tau}} = \mu_{eff}\left[\left(\nabla \vec{v_g} + \nabla \vec{v_g}^T\right) - \frac{2}{3}\nabla \cdot \vec{v_g} I\right] \tag{4}$$

where I is the unit tensor. μ_{eff} is the effective dynamic viscosity, which is the sum of the molecular viscosity μ and the turbulent viscosity μ_t.

The species transport equation is

$$\frac{\partial}{\partial t}(\rho_g Y_i) + \nabla \cdot (\rho_g \vec{v_i} Y_i) = -\nabla \cdot \vec{J_i} + R_i + S_i \tag{5}$$

where Y_i and $\vec{v}_i$ are the local mass fraction and velocity of species i. There is no chemical reaction in this study, so R_i, the net production rate of species i, is constantly zero. S_i, the

rate of additional creation of species i from the dispersed phase, is also constantly zero in this study.

Mass diffusion due to gradients in concentration and temperature is modeled by Fick's law. $\vec{J}_i$ is the diffusion flux of species i, which can be written as

$$\vec{J}_i = -\left(\rho_g D_{i,m} + \frac{\mu_t}{Sc_t}\right)\nabla Y_i - D_{T_g,i}\frac{\nabla T_g}{T_g} \tag{6}$$

$D_{i,m}$ is the mass diffusion coefficient for species in the mixture [46], which is defined by

$$D_{i,m} = \left(\sum_{j,j\neq i}\left(\frac{X_j}{D_{ij}}\right) + \frac{X_i}{(1-Y_i)}\sum_{j,j\neq i}\left(\frac{Y_j}{D_{ij}}\right)\right)^{-1} \tag{7}$$

Sc_t is the turbulent Schmidt number, defined as 0.7 in this study. X_i is the mole fraction of species i in the mixture. $D_{T_g,i}$ is the thermal diffusion coefficient, and T_g is the local temperature. D_{ij} is the binary mass diffusion coefficient of species i in species j.

3.2. Turbulence Model of Continuity Phase

The Shear-Stress Transport (SST) $k-\omega$ turbulence model is a popular two-equation eddy-viscosity model used in computational fluid dynamics to simulate turbulent flows [47]. This study chooses the SST $k-\omega$ model as the continuous phase's turbulence model. The specific equations are as follows [48].

The transport equation of turbulence kinetic energy, k, is

$$\frac{\partial}{\partial t}(\rho_g k) + \frac{\partial}{\partial x_i}(\rho_g k\vec{v_g}) = \frac{\partial}{\partial x_j}\left(\Gamma_k\frac{\partial k}{\partial x_j}\right) + G_k - Y_k + S_k \tag{8}$$

The transport equation of the specific dissipation rate, ω, is

$$\frac{\partial}{\partial t}(\rho_g \omega) + \frac{\partial}{\partial x_i}(\rho_g \omega\vec{v_g}) = \frac{\partial}{\partial x_j}\left(\Gamma_\omega\frac{\partial \omega}{\partial x_j}\right) + G_\omega - Y_\omega + S_\omega \tag{9}$$

Γ_k and Γ_ω are the effective diffusivity for k and ω, respectively. G_k and G_ω represent the generation of k and ω, while Y_k and Y_ω represent the dissipation of k and ω. In addition, S_k and S_ω are the source terms of k and ω from the dispersed phase, respectively.

3.3. Governing Equations of Dispersed Phase

In this study, the motion of the particles is described using the Lagrangian reference frame. The interactions between particles are not considered because the volume fraction of particles in this study is $\ll$0.1%.

The force balance equation for the particle can be written as

$$m_p\frac{\partial\vec{v_p}}{\partial t} = \vec{F_d} + \vec{F} \tag{10}$$

$\vec{F_d}$ is the drag force of the particle, which can be calculated by

$$\vec{F_d} = m_p\frac{3\mu C_D Re_p}{4\rho_p {d_p}^2}(\vec{v_g} - \vec{v_p}) \tag{11}$$

Re_p is the relative Reynolds number of the particle, which can be calculated by

$$Re_p = \frac{\rho_g d_p|\vec{v_p} - \vec{v_g}|}{\mu} \tag{12}$$

C_D is the drag coefficient of the particle, which is highly sensitive to Re_p. Spherical fuel possesses excellent fluidization properties [49] and has been widely applied in the supply systems of powdered fuels [50]. In this study, the powder fuel is assumed to be spherical, and C_D can be calculated by

$$C_D = \begin{cases} \frac{24}{Re_p}\left(1 + \frac{Re_p^{0.675}}{6}\right) & Re_p < 1000 \\ 0.46 - \frac{400}{Re_p}\exp\left(-\left(\log\left(\frac{Re_p}{8000}\right)\right)^2\right) & Re_p \geq 1000 \end{cases} \tag{13}$$

$\vec{F}$ represents other interaction forces. Considering the strong shear effects and strong discontinuities of supersonic flow in this study, the pressure gradient force and Saffman's lift force [51,52] are considered part of $\vec{F}$, which can be calculated as follows

$$\vec{F}_{\text{pressure gradient}} = m_p \frac{\rho_g}{\rho_p} \vec{v_g} \nabla \vec{v_g} \tag{14}$$

$$\vec{F}_{\text{Saffman's lift force}} = m_p \frac{2K\nu^{1/2}\rho_g d_{ij}}{\rho_p d_p (d_{lk} d_{kl})^{1/4}} (\vec{v_g} - \vec{v_p}) \tag{15}$$

where K is a constant defined as 2.594 and d_{ij} is the deformation tensor. ν is the kinematic viscosity. Other forces acting on the particles, such as the Magnus lift force and virtual mass force, are neglected as their effects are minor or incompatible with this study. Phase changes or chemical reactions of particles are not considered. Interactions between particles and the wall, such as deceleration and deformation, are also not considered. The collisions between particles and the wall are treated using an ideal, fully elastic collision model. These treatments simplify the problem and allow for a focus on the primary dynamics of particle motion in the flow field.

The heat balance equation for the particle can be written as

$$m_p c_p \frac{\partial T_p}{\partial t} = h A_p (T_g - T_p) + \epsilon_p A_p \sigma ({\Theta_R}^4 - {T_p}^4) \tag{16}$$

where c_p and A_p are the heat capacity and surface area of the particle. T_g is the temperature of the continuous phase. h and σ are the convective heat transfer coefficient and Stefan–Boltzmann constant. ϵ_p is the particle emissivity, and Θ_R is the radiation temperature.

This study employed the method of mesh node averaging to ensure a smoother solution of the source terms, distributing the influence of discrete-phase parcels more evenly to neighboring cells to achieve smooth and accurate computation results. The averaging equation for the source terms of the discrete-phase parcels is as follows

$$\overline{\phi}_{\text{node}} = \sum_n N_{\text{in parcel}} w \left(\frac{\vec{x}_p^n - \vec{x}_{\text{node}}}{\Delta x} \right) \phi_p \tag{17}$$

In this equation, $\overline{\phi}_{\text{node}}$ represents the accumulation of the particle variable on the node for all parcels n. $N_{\text{in parcel}}$ denotes the number of particles in the parcel, while w is the weighting function, also referred to as the kernel. The position of the particle is given by $\vec{x}_p^n$, and the position of the node is indicated by $\vec{x}_{\text{node}}$. The characteristic length scale of the cell containing the parcel is represented by Δx, and ϕ_p denotes the particle variable.

The kernel function used in this study is the Gaussian method, and its weighting equation is as follows [53,54]

$$w\left(\frac{\vec{x}_p - \vec{x}_{\text{node}}}{\Delta x}\right) = \left(\frac{a}{\pi}\right)^{3/2} \exp\left(-a\left(\frac{|\vec{x}_p - \vec{x}_{\text{node}}|}{\Delta x}\right)^2\right) \quad (18)$$

where a is the parameter that controls the width of the Gaussian distribution.

Considering its advantages in handling high-speed compressible flows, this study used a density-based solver. Implicit formulations were employed to solve the steady-state flow field. The Advection Upstream Splitting Method Plus (AUSM+) flux scheme [55] and second-order upwind discretization methods were used for the computations. For gradient evaluation, the cell-based least square method was applied [56]. Additionally, this study used the net mass flow rate as a key convergence criterion. The calculation was considered converged when the residuals in the computational domain were stable, and the thousand-step average of the net mass flow rate was less than 1% of the minimum inlet flow rate [43].

3.4. Validation of Numerical Methods

The governing equations of the continuous phase, turbulence, and dispersed phase are validated before the formal simulation work to ensure the accuracy and reliability of this study's numerical models and methods. The details of related validations are presented in this section.

3.4.1. Validation of Continuous Phase

The continuous phase and turbulence validations are based on the studies conducted by F. W. Spaid and E. E. Zukoski [57,58]. The experimental cases involve the sonic injection of a nitrogen jet through a transverse slot nozzle in the wall into a supersonic airflow. The validation cases determine the accuracy of the simulation model by comparing the wall pressure coefficient measured in the experiments. This wall pressure coefficient is defined as the ratio of the local static pressure to the static pressure at the inlet, P/P_∞. The numerical simulations use conditions from experiment cases 10 and 11, corresponding to case a and case b, respectively. In these cases, with an incoming Mach number, Ma_∞ of 3.50, the ratios of the total pressure of the slot nozzle to the static pressure of the incoming flow, $P_{0,j}/P_\infty$, are 16.55 and 32.40, respectively.

The comparison results are shown in Figure 2. The coefficient of determination (R^2) evaluates the explanatory power of the model on the overall variance of the data. At the same time, the mean absolute percentage error (MAPE) measures the overall relative error between the predicted and actual values. In this study, the R^2 for case a is 0.994, and the MAPE is 2.65%, while the R^2 for case b is 0.996, and the MAPE is 2.16%, both meeting the precision requirements. Thus, this study's numerical simulation models and methods used for the continuous phase are considered compatible and reliable for a jet flow field in a supersonic flow.

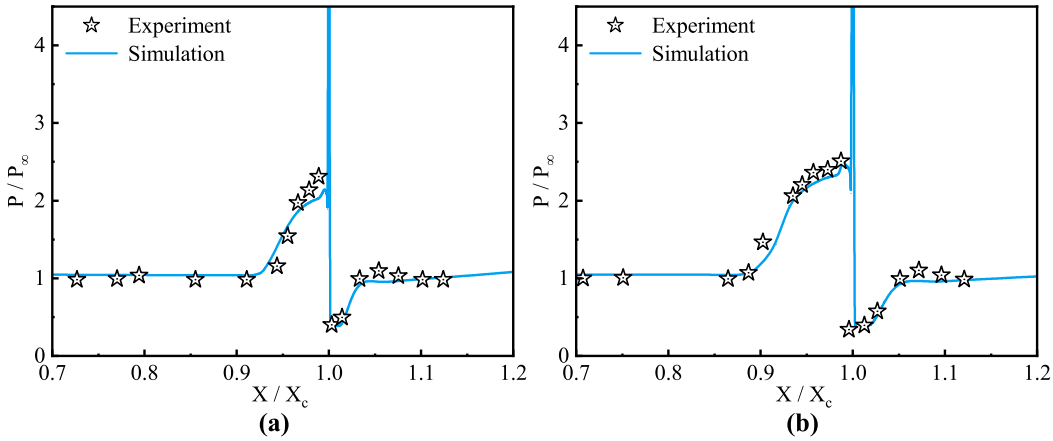

Figure 2. Comparison of pressure distribution along the wall between experiment and simulation: (**a**) $P_{0,j}/P_\infty$ = 16.55; (**b**) $P_{0,j}/P_\infty$ = 32.40.

3.4.2. Validation of Dispersed Phase

The validations of the dispersed phase are founded on the studies conducted by M. Sommerfeld [59]. His experiments investigated the motion of particles in a gas–solid two-phase coupled flow injected into a low-pressure chamber. The static pressure in the chamber was about 10 kPa. Air served as the gas phase, and the particles were spherical glass beads with a density of 2500 kg/m^3. The velocities of the particles at various positions along the nozzle axis were measured using APD and other equipment. The two simulation cases in this section are derived from these experiments. In case c, the particle diameter D_p is set to 26 μm and the particle loading ratio η, defined as $\eta = \dot{m}_p/\dot{m}_g$, is set to 0.39. The P_0 of the gas is set to 98 kPa (0.980 bar). In case d, the particle diameter D_p is set to 45 μm, the particle loading ratio η is set to 0.25, and P_0 is set to 310.5 kPa (3.105 bar).

The comparison results are shown in Figure 3, with case c corresponding to (a) and case d corresponding to (b). In the simulation cases, many particles are along the nozzle axis, so multiple points are statistically analyzed in the figure. The results indicate that the experimental data match the points in the numerical simulation results, validating the numerical simulation's effectiveness in predicting particle motion. Thus, the numerical simulation models and methods of the dispersed second phase used in this study are considered compatible and reliable.

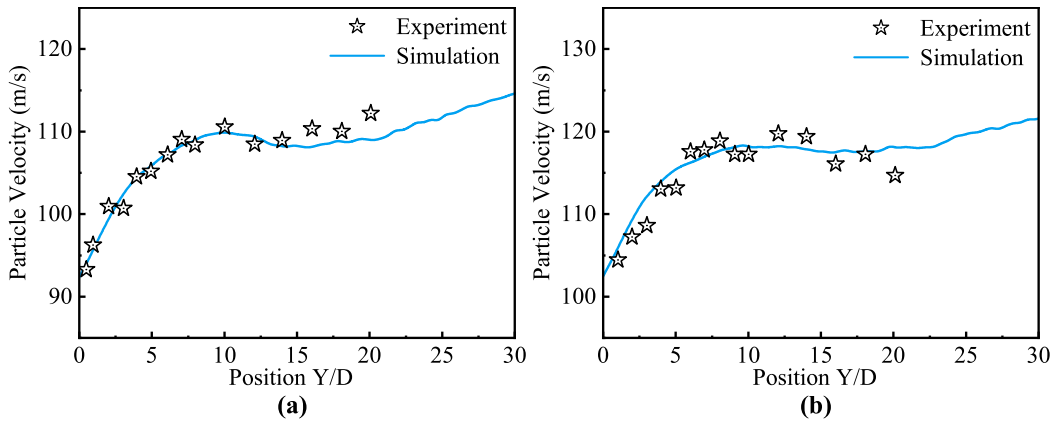

Figure 3. Comparison of particle velocity distribution along the centre of the injector between experiment and simulation: (**a**) D_P = 26 μm, η = 0.39, P_0 = 0.980 bar; (**b**) D_P = 45 μm, η = 0.25, P_0 = 3.105 bar.

3.5. Grid and Independence Verification

In this study, 3D grids are generated using ANSYS ICEM. Considering the computational time and resource limitations, the computational domain is divided along the Z symmetry plane, and only half of the domain is modeled. The grid and boundary conditions of the computational domain are shown in Figure 4.

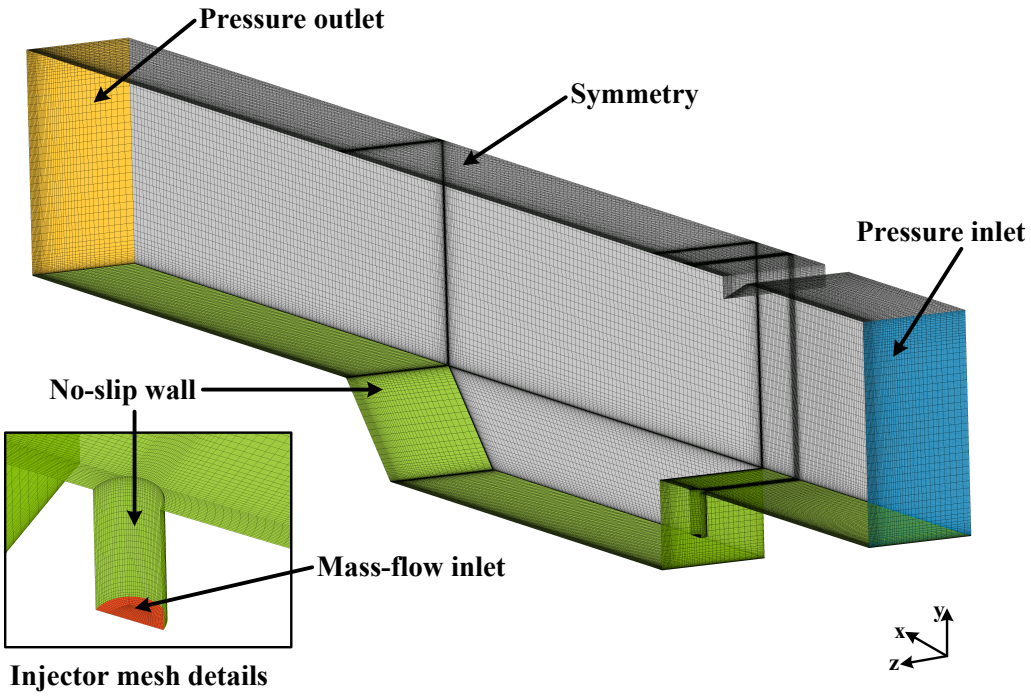

Figure 4. Grids and boundary conditions of computation region.

Three sets of grids with different levels of refinement were generated for validation to ensure the reliability of the computational results and the independence of the grid. The grid numbers for the three sets are about 0.65 million, 1.35 million, and 2.68 million, respectively. Details of the grids are shown in Table 4, and the validation results are shown in Figure 5. After the three sets of grids converged, the y^+ was close to 1 in most areas. This indicates that the grids are suitable for the near-wall treatment method without wall functions of the SST $k-\omega$ model. The moderate and refined grids' results were generally consistent when comparing the pressure coefficients on the top and bottom walls. Therefore, this study used the moderate grid as the computational grid.

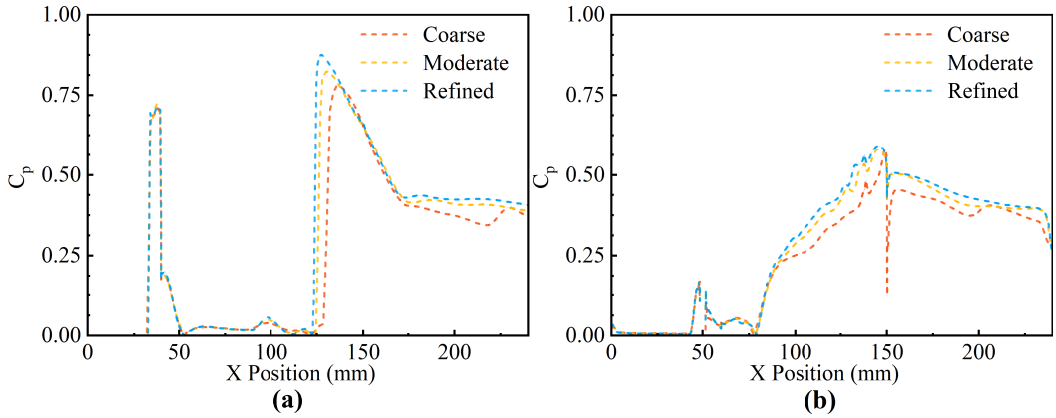

Figure 5. Wall pressure coefficient distribution with grids of different fineness levels: (**a**) top wall; (**b**) bottom wall.

Table 4. Details of grids.

	N_x	N_y	N_z	Number of Nodes
Coarse grid	266	59	39	647,414
Moderate grid	374	72	48	1,350,816
Refined grid	481	86	64	2,684,070

4. Results and Discussion

4.1. Effect on Shock Wave Structures

In the supersonic combustion chamber, jets oriented perpendicular to the incoming flow always induce complex shock wave structures. Besides these wave structures, this study also introduces induced shock waves from the ramp on the top wall into the supersonic flow fields. The two sets of shock wave structures couple in the combustion chamber, forming more complex wave structures. Numerical Schlieren is a computational visualization technique to capture and analyze variations in fluid density and flow structures by visualizing the refractive index gradients in the simulated fluid [60]. As shown in Figure 6, the numerical Schlieren results illustrate the field structures in the centrosymmetric section (Z = 0), providing a clearer view of the evolution of shock waves in the combustion chamber as the solid-to-gas ratio changes. When ζ exceeds 1.0, the mass flow ratio between the jet and the mainstream is very low, resulting in weaker shock wave structures generated by the jet. The main shock wave structures in the combustion chamber are the induced shock waves from the top wall. The lambda shock remains close to the jet inlet with limited influence, while the bow shock is of a low height and has limited impact, too. The induced shock waves work directly on the leading edge of the cavity. As ζ decreases, the intensity of the lambda shock grows, and its position shifts upstream. Concurrently, the heights of the bow and barrel shocks also increase. When ζ falls below 1.0, the bow shock and barrel shock begin to interact with the induced shock waves from the top wall. The interaction between the induced shock and the bow shock leads to the induced shock propagating in alignment with the bow shock. Consequently, it ceases to impact the flow field at the cavity's leading edge. The shock wave structures generated at the trailing edge of the transitional cavity produce reflected shock waves on the top wall in the mid-rear section of the combustion chamber. As ζ continues to decrease, the impact points of these reflected shock waves gradually move forward. Their intensity steadily diminishes as the velocities near the trailing edge of the cavity decrease.

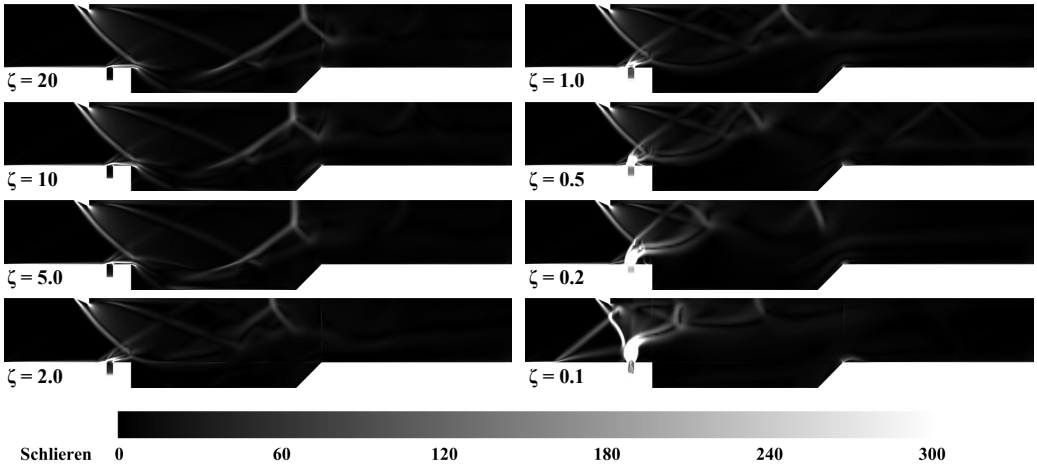

Figure 6. The numerical Schlieren results on the centrosymmetric section (Z = 0) with different ζ values.

Another series of numerical Schlieren results illustrate the field structures at the Y = 0 section from top views, as shown in Figure 7. These results provide a more intuitive observation of the evolutionary patterns of lambda shocks, bow shocks, barrel shocks, and the induced shocks from the top wall under different solid-to-gas ratios. It can be seen that there are three layers of shocks observed along the flow direction, the lambda shock, bow shock, and barrel shock in succession, taking the numerical Schlieren result of $\zeta = 1.0$ as an example. It can be noted that when ζ exceeds 1.0, the lambda shock is weak and mostly coincides with other shocks, observing the changes in shock wave structures under different solid-to-gas ratios. As ζ decreases, indicating an increase in the jet's mass flow rate, the size and intensity of the bow shock continuously enhance. Conversely, when ζ drops below 1.0, the lambda shock separates from the coupled shocks and moves forward, increasing in intensity. Similarly, the intensity of the bow shock and barrel shock grows with the decreasing ζ, and their heights at the same position increase. This makes it difficult to see their subsequent development in the Y = 0 section. However, the evolution of these shock wave structures' intensity can still be inferred from the Schlieren results behind the cavity along the streamwise direction. Under lower ζ, the Schlieren intensity behind the cavity's trailing edge is higher, indicating that the intensity of the shock wave structures in this region is also higher. Additionally, the numerical Schlieren results with ζ values of 20, 10, and 5.0 show an additional curved shock wave structure in the mid part of the cavity. This structure results from the coupling effect combined with the results in Figure 6. This coupling effect occurs between the reflected shock wave at the trailing edge of the cavity and the shock wave generated behind the ramp on the top wall. Consequently, this shock strengthens with the increased intensity of the reflected shock when ζ is more significant than 5.0. However, with even lower ζ, the velocities of incoming flow reaching the cavity's trailing edge decrease, reducing the intensity of the reflected shock waves, thereby weakening and eventually eliminating this coupling effect.

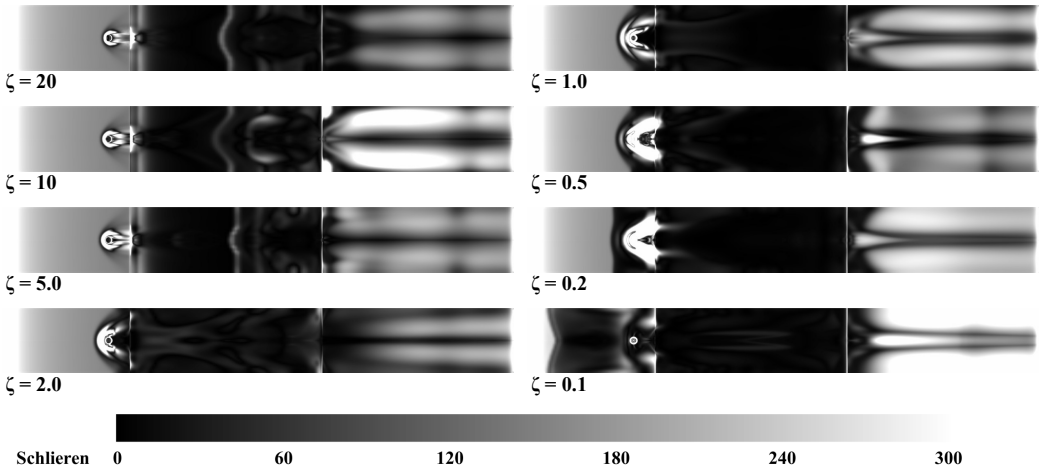

Figure 7. The numerical Schlieren results on the top section (Y = 0) with different ζ values.

The Mach number distribution on the centrosymmetric section (Z = 0) is shown in Figure 8, providing a more precise visualization of how the induced shock waves influence the flow fields. The incoming flow has a Mach number of 2.40, and under an approximately 50° induced shock wave, the Mach number of the post-shock flow is around 1.40. Similar to the evolutionary patterns shown in the Schlieren images (Figure 6), when ζ exceeds 1.0, the induced shock waves significantly impact the flow structures at the cavity position. This impact generates a high-speed region in the front-mid part of the cavity. This phenomenon causes the shear layers above the cavity to move significantly downward and backward, and the incoming flow at the leading edge of the cavity exhibits a strong downward

movement trend. In such a flow field, the shock waves that influence the particles are more likely to be the induced shock waves from the top wall, the reflected shock waves from the trailing edge of the cavity, and their coupled structures. When ζ is lower than 1.0, the induced shock waves struggle to affect the cavity's leading edge directly. The strengthening bow shock waves and barrel shock waves from the jet cause the shear layers of the cavity to move upward as ζ decreases, and the low-speed region extends upstream as well. This phenomenon further reflects the evolutionary patterns of the reflected shock waves at the trailing edge of the cavity mentioned in Figure 7. Under lower ζ, the low-speed region above the cavity develops upwards, covering the geometric trailing edge of the cavity. This change in the low-speed region significantly reduces the velocity of the incoming flow at the trailing edge of the cavity, even to subsonic levels. As a result, the intensity of the reflected shocks on the upper wall is continuously weakened. Comparing the Mach number distribution in Figure 8 for ζ values of 1.0, 0.5, 0.2, and 0.1, the coupling positions of the induced shock waves from the ramp and the shock waves generated by the jet are noted to be different, leading to complex shock structures with different evolutionary processes. In the case with a ζ of 0.1, the significant enhancement and forward movement of the lambda shock waves cause the coupling between them and the induced shock waves to begin much earlier. This coupling further enhances the bow shock from the jet. These structures collectively bring the flow field into a lower-speed state earlier. In such a flow field, the influence on particles is likely a combined effect of the coupling structures of the shock waves from jets and the induced shock waves from the top wall.

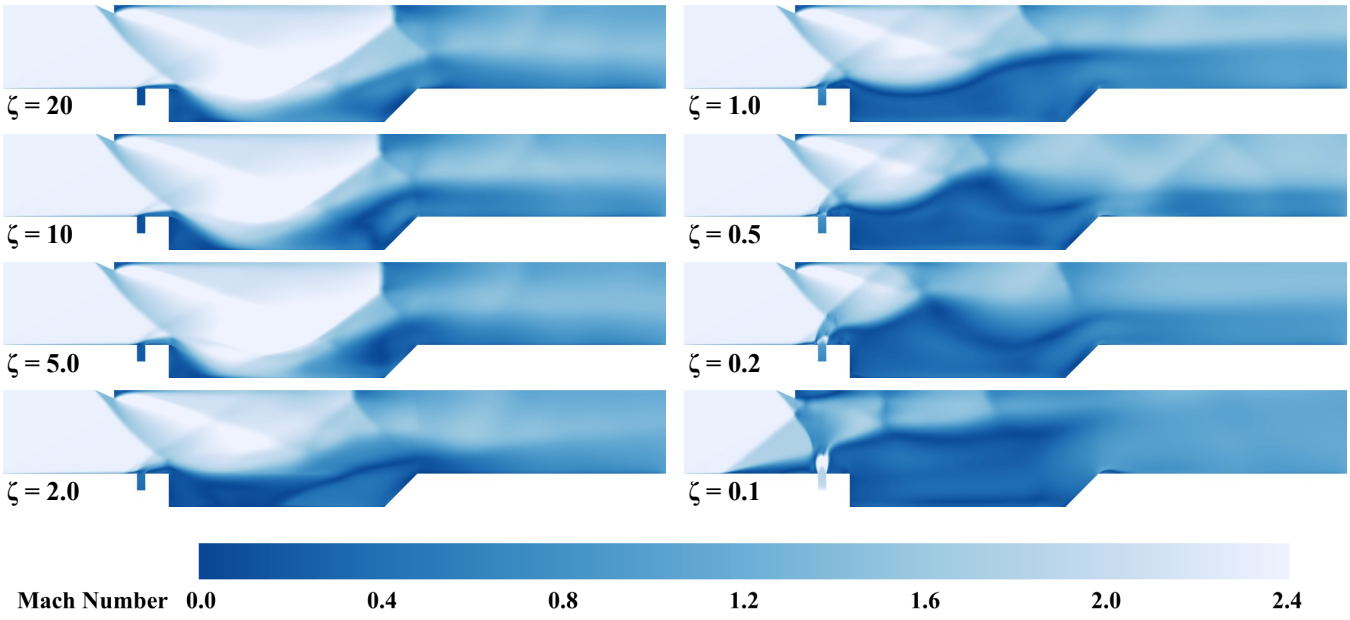

Figure 8. The distribution of Mach number on the centrosymmetric section (Z = 0) with different ζ values.

The statistical analysis of the flow fields along the streamwise direction is presented in Figure 9, focusing primarily on the distribution of velocity and turbulent kinetic energy. It is evident that, with lower ζ, the velocity in the flow field experiences a more significant decrease earlier along the streamwise direction. As ζ increases, this effect diminishes. When ζ is greater than 1.0, the velocity in the flow field shows a notable increase in the regions between X = 60 mm and X = 120 mm, which correspond to the cavity structure. The flow acceleration is likely due to the sudden expansion of the cavity. However, this effect is less pronounced at lower ζ. At X = 50 mm, the flow field velocity reaches the first trough for all cases. X = 50 mm is the position of the fuel jet, indicating significant energy

exchange between the jet or particles and the incoming supersonic flow. It can be inferred that the substantial influence arises from energy and momentum exchange between the jet and the incoming supersonic flow by comparing the results between different ζ values. In other words, the jet impacts the initial velocity of the incoming flow as it develops downstream, altering the flow field structure. By comparing the outlet velocity distribution of the combustion chamber, it can be noted that the highest outlet velocity occurs at a ζ of 1.0. This could be attributed to the excessive impact of the cavity on the incoming flow at lower solid-to-gas ratios. In comparison, higher solid-to-gas ratios affect the initial velocity of the incoming flow, leading to this phenomenon.

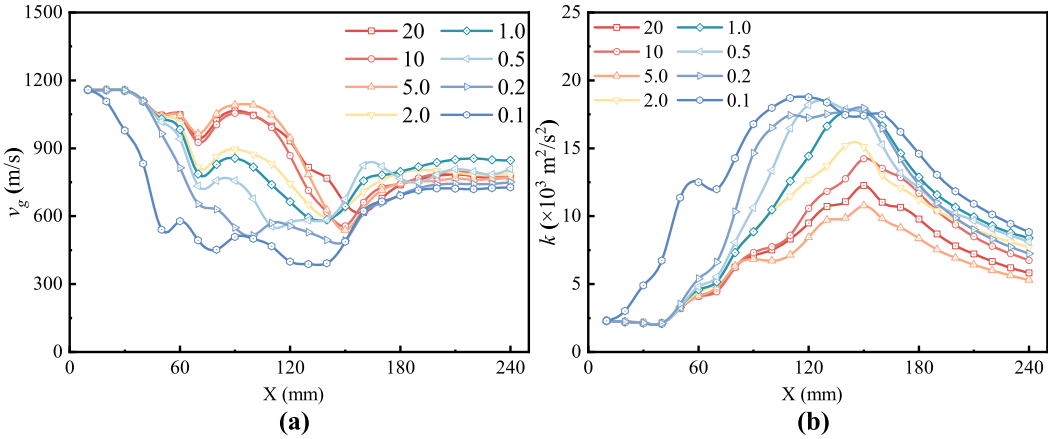

Figure 9. Average value of (**a**) velocity and (**b**) turbulent kinetic energy along the streamwise direction with different ζ values.

The solid-to-gas ratio significantly influences shock wave behavior in supersonic combustion chambers. When the ratio exceeds 1.0, induced shock waves from the top wall dominate. With a decreasing ratio, the intensity and position of lambda, bow, and barrel shocks change, leading to complex shock interactions. These interactions become more pronounced at lower ratios, significantly altering the flow field. At higher ratios, induced shock waves mitigate the strong shear effects from the cavity while intensifying the coupling of reflected shock waves at the trailing edge. The flow field shows a significant downward movement above the cavity. At lower ratios, induced shock waves couple with jet-generated shock waves, amplifying shear effects and decreasing the flow field velocity.

4.2. Effect on Vortex Structures

The distribution of the vorticity magnitude on the centrosymmetric section (Z = 0) with different solid-to-gas ratios is shown in Figure 10. Generally, high-vorticity regions indicate the presence of large-scale vortices. The rotational areas around these large-scale vortices can significantly influence fuel dispersion. By combining with previous flow field structure analysis, it can be observed that high-vorticity regions appear at the interfaces between high-speed and low-speed areas. These high-vorticity regions suggest the presence of large-scale vortex structures, where intense rotational motion exists at the edges of the shear layers, significantly affecting fuel dispersion.

The distribution of turbulent kinetic energy on the centrosymmetric section (Z = 0) with different solid-to-gas ratios is illustrated in Figure 11. From the previous analysis, similar to the vorticity distribution, high-shear regions exhibit high turbulent kinetic energy levels. As many studies have shown, this phenomenon indicates that large-scale vortices are generated by high fluctuations and flow instability, significantly enhancing the mixing efficiency of liquid or gaseous fuels. Notably, some low-speed regions have low vorticity but high turbulent kinetic energy. These regions may not have large-scale vortex structures

but might have small-scale or broken vortices. These small-scale vortex fluctuations can still impact powder fuel flow and mixing processes, enhancing fuel dispersion. In this study, as ζ decreases, the distribution of turbulent kinetic energy broadens and reaches higher peak values. The changes in the distribution suggest that the small-scale vortex fluctuations in these regions become more intense. At lower ζ values, the shock wave structures in the supersonic combustion chamber become more intricate, enhancing the interactions between shock waves. It could be one reason for the increased turbulent kinetic energy and instability. The spatial extent of regions with high turbulent kinetic energy increases, leading to more substantial and widespread small-scale vortex fluctuations in the flow field. These regions are likely to promote more effective mixing and interaction of the fuel particles with the incoming flow, potentially enhancing the combustion process.

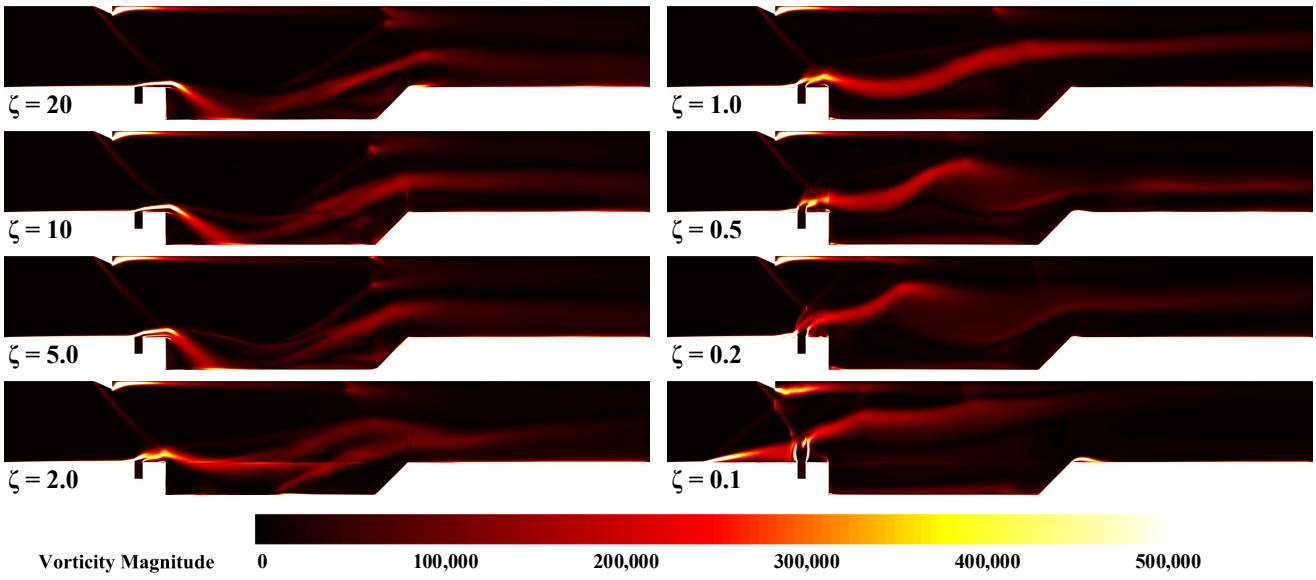

Figure 10. The distribution of vorticity magnitude on the centrosymmetric section (Z = 0) with different ζ values.

The statistical analysis of turbulent kinetic energy levels is shown on the right side of Figure 9. High levels of turbulent kinetic energy are concentrated in the regions between X = 60 mm and X = 180 mm, which includes the cavity and some downstream areas. It is indicated that strong shear effects significantly impact turbulent kinetic energy levels. Notably, at a ζ of 0.1, turbulent kinetic energy levels rise earlier, likely due to the upstream development of the lambda shock. This upstream development alters previously established turbulent kinetic energy levels through strong discontinuities. Additionally, for a ζ of 5.0, turbulent kinetic energy levels remain consistently lower, and the flow field's velocity along the flow direction is higher compared to other cases in the first half. These characteristics suggest that this flow field is less favorable for powder fuel's diffusion and mixing process. Through the flow field structures, the coupling shock waves might impact the sloped surface at the trailing edge of the cavity. This results in the shock wave developing downstream, coupling with its reflected shock wave but with both shock waves weakening each other. Consequently, the reflected shock structures weaken the overall effectiveness of the shock waves on the flow field.

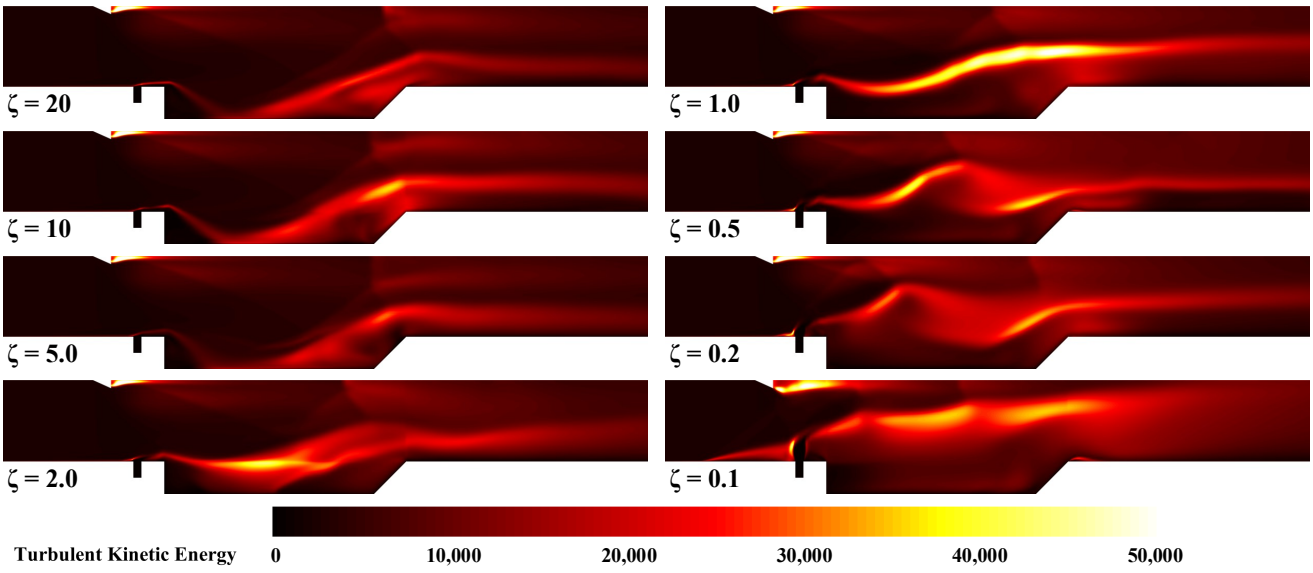

Figure 11. The distribution of turbulent kinetic energy on the centrosymmetric section (Z = 0) with different ζ values.

The Omega criterion is used to identify the vortex structures, with the characteristic value set at the conventional 0.52. The identified vortex structures, colored by local vorticity magnitude, are depicted in Figure 12a. Observations near the jet nozzle indicate that as ζ values decrease, the lambda shock intensifies and develops upstream. Prominent barrel and bow shocks emerge when ζ reduces to 2.0 or lower, increasing their intensities and heights as previously discussed. These barrel and bow shocks impact the vortex structures in the front part of the cavity. At higher solid-to-gas ratios, enhanced triangular swirling vorticity forms at the front part of the cavity. Conversely, these triangular vorticities extend backward at lower ratios, filling the cavity. Notably, at a ζ of 5.0, the number of vortex structures within the cavity is substantially lower, with a narrower distribution in the Z-direction compared to other cases. The number of vortex structures is significantly reduced even in the area behind the cavity.

Two-dimensional cuts of the vortex structures taken along the streamwise direction are shown in Figure 12b. The cuts are located at X = 80, 120, 160, and 200 mm, corresponding to the cavity's front, rear, and behind regions and just before the outlet of the chamber, respectively. This section explores the evolution of the vortex structures. At higher solid-to-gas ratios, vortex structures develop at lower heights. When ζ exceeds 5.0, the vortex core positions at X = 80 mm and X = 120 mm are below Y = 0, indicating that the vortex cores descend into the cavity, while the upper limit of the vortices aligns along the shear layer height. At lower solid-to-gas ratios, vortex structures generally develop above the Y = 0 plane and form multiple vortex cores in the Y-direction in several cases. The upper limits of the vortex structures still develop along the shear layer height, and the distribution area of high-level vortices downstream of the cavity increases significantly. Additionally, the vortex structures begin to expand significantly in the Z-direction, with the rotational regions of the vortices gradually expanding to fill the entire Z-direction flow field as ζ decreases. Interestingly, as shown in Figure 12a, the overall vortex level of the flow field is lower at a ζ of 5.0, leading to an abnormal phenomenon in particle distribution, which will be discussed in the next section.

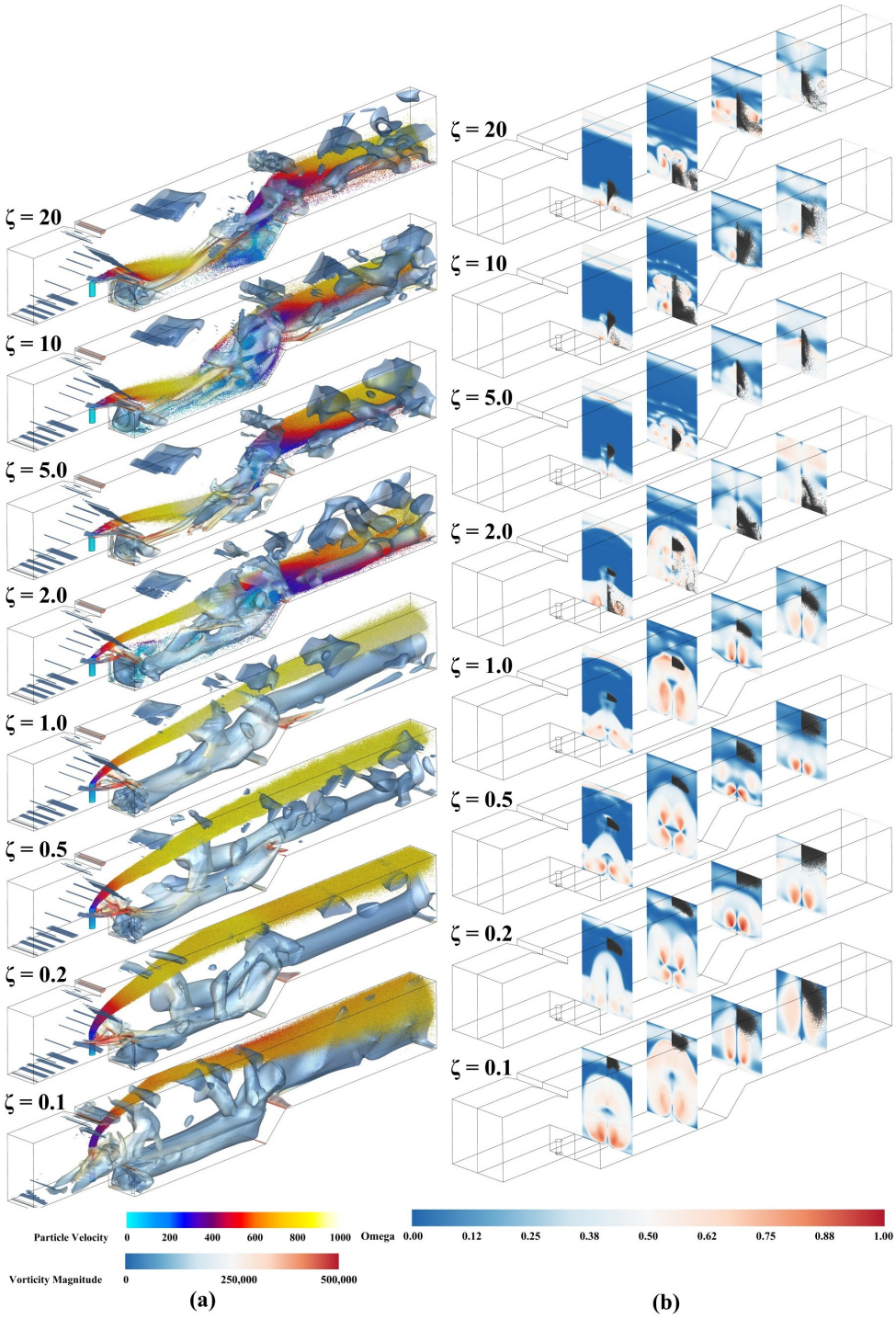

Figure 12. (**a**) The vortex structures identified via the Omega method ($\Omega = 0.52$) and the distribution of particles with different ζ values. The 3D vortex structures are colored with vorticity magnitude, and the particles are colored by their velocity. (**b**) The distribution of particles and 2D cuts of vortex structures identified via the Omega method ($\Omega = 0.52$) on the streamwise sections (x = 80, 120, 160, 200 mm) with different ζ values.

4.3. Effect on Flow Process of Powder Fuel

This section primarily discusses particle motion states and distributions in a supersonic flow field. Through a thorough analysis of the distribution of particles in different directions,

this section aims to explore particle behavior and its connection with flow structures, particularly vortex structures, in the supersonic combustion chamber.

The relationship between particle distributions and vortex structures is also illustrated in Figure 12a, focusing on vorticity structures that directly interact with particles. As particles pass through vortex structures, their velocities decrease significantly, which enhances diffusion along the vorticity. This effect is particularly pronounced at ζ values of 20, 10, 5.0, and 2.0. At higher solid-to-gas ratios, particles primarily move above the vorticity in the cavity and downstream regions, thus preventing diffusion along the vorticity. However, when particles enter the vortex influence region, such as at a ζ of 0.1, the enhanced diffusion effect of the vortex structures on the particles becomes significant.

Several 2D cuts of vortex structures and the particle distribution for a more detailed analysis of their relationship are shown in Figure 12b. Particles closely align with the vortex structures at higher solid-to-gas ratios, such as 20, 10, 5.0, and 2.0. In regions with high Omega values, particles diffuse along vortex structures in the Z-direction. It is indicated that at these solid-to-gas ratios, vortex structures significantly guide and influence particle movement. As ζ decreases further, particles move away from regions where vortex structures develop. For example, at ζ values of 1.0 and 0.5, particles predominantly move in the regions above the vortex structures, showing lower diffusion along the Z-direction than regions within the vortex structures. When particles do not enter the vortex development region at the initial stage, the rotational effect of the airflow along the vortex core continuously excludes them from the rotational region. This exclusion causes particles to develop significantly along the vortex boundary. When ζ decreases to 0.2 and 0.1, as the vortex structures develop upward, particles re-enter the vortex regions in the mid-rear part of the chamber. In these cases, particle diffusion in the mid-rear flow is unexpectedly higher than under conditions with larger solid-to-gas ratios. Unlike previous cases, particles are forcibly pressed into the vortex development region. Although the rotational motion along the vortex core is still ongoing, since the particles have already entered the rotational region, the airflow can only entrain the particles and continue to develop them towards the outer rotational region, which enhances particle diffusion. This analysis indicates that vortex structures significantly influence particle diffusion and enhance mixing. Particles must couple with the rotational regions of vortex structures directly to achieve more substantial diffusion or enhanced mixing. This coupling can be achieved by inducing more vortex structures within particle distribution regions or by forcing particles into vortex regions.

The distribution of particles and jet gas (N_2) in the centrosymmetric section (Z = 0) with different solid-to-gas ratios is shown in Figure 13. The particles, colored by their velocity, clearly compare distribution patterns along the streamwise direction in different cases. When ζ values are 10.0 and 20.0, particles enter the cavity with the flow field and form a swirling flow, leading to particle retention. As ζ decreases to 5.0, particles pass through the cavity but are deflected by the inclined surface at the trailing edge of the transitional cavity, preventing them from remaining in the cavity. They are directly reflected back into the incoming flow, continuing their downstream journey. With a further reduction in ζ, particles enter the mainstream with increasingly higher initial velocities and penetration depths, preventing them from entering the cavity or shear layer. On the other hand, the distribution of jet gas (N_2) is shown in the exact figures. The distribution of N_2 is directly related to the shear layer boundaries, with high concentrations appearing at the interfaces between high-speed regions and low-speed regions, covering the entire shear-layer regions. Comparing the particle and N_2 distributions, it is clear that the wave structures influence particles in the flow. For instance, at a ζ of 0.5, downstream shock waves from the jet nozzle create significant disturbances, which are reflected in the subsequent evolution patterns of particle motion.

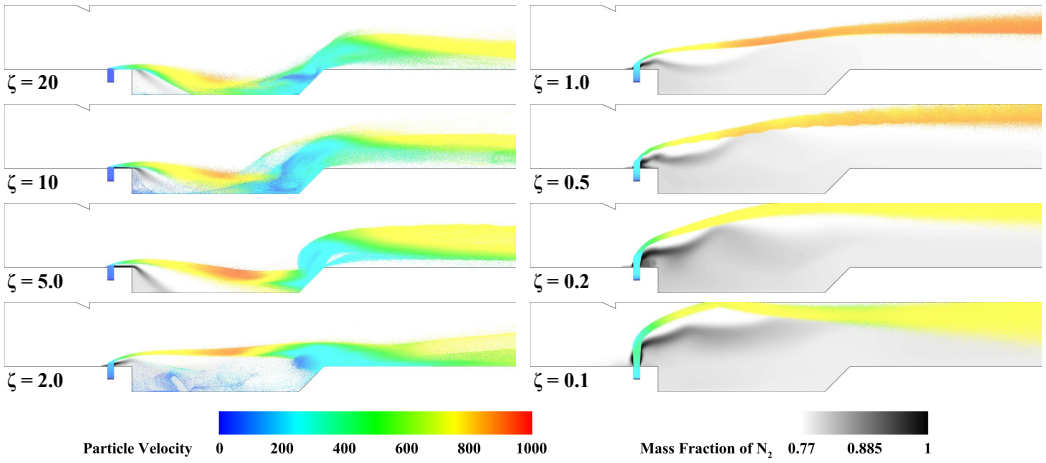

Figure 13. The distribution of particles and jet gas (N_2) in the centrosymmetric section (Z = 0) with different ζ values. The particles are colored with their velocity.

Additionally, particles exhibit strong lag effects in response to the flow field, while the diffusion of N_2 occurs almost without delay. Under the same conditions, changes in particle motion always lag behind those of N_2, and this lag increases with higher solid-to-gas ratios. When particles enter the shear layer due to effects like wall reflection, their distribution and velocity will change. At a ζ of 1.0, particles do not enter the shear layer, resulting in minimal diffusion along the Y-direction and the highest average velocity at the combustion chamber outlet. Conversely, at a ζ of 0.1, particles reach the top wall earlier and are reflected into the shear layer, significantly increasing their diffusion along the Y-direction. Pulsations within the shear layer affect the downstream velocity development of the particles, significantly reducing their velocity at the outlet of the combustion chamber. Figure 14 shows the average velocity statistics of particles along the flow direction. The statistical results corroborate the previous analysis, confirming the trends in particle motion at different solid-to-gas ratios.

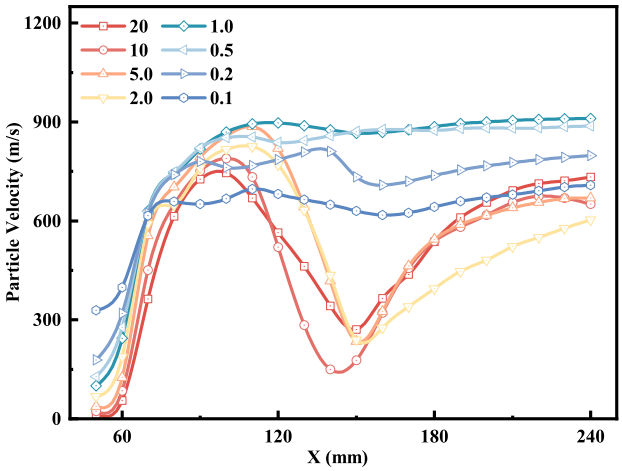

Figure 14. Average values of particle velocity along the streamwise direction with different ζ values.

This study conducts a detailed statistical analysis of particle diffusion behavior, focusing on the particles' geometric center and maximum diffusion depth in both Y- and Z-directions, with particular attention to their evolution along the streamwise direction. Figure 15 displays the average value of the geometric center and diffusion depth of particles in the Y-direction along the streamwise direction with different solid-to-gas ratios. Regarding the geometric center of the distribution, it is evident that particles with high solid-to-gas ratios enter the cavity under the influence of induced shocks. When ζ is greater than 2.0, the

geometric center of the particles appears within the regions between −12 mm and 0 mm. Without considering the rebound effect from the wall, as ζ decreases, the geometric center of the particles continuously increases, indicating an upward development in particle distribution. The trends in maximum diffusion depth, which refers to the penetration depth, are similar to those of the geometric center. However, the X position, where the minimum diffusion depth occurs, differs at high solid-to-gas ratios. This phenomenon occurs because the strong interaction points between the wave structures and particles develop downstream as ζ decreases. When ζ exceeds 5.0, particles experience a rebound effect from the cavity's rear edge. Consequently, in the combustion chamber beyond X = 150 mm, the particles' geometric center and diffusion depth are higher compared to cases with ζ of 2.0 or lower, where the particles do not enter the cavity.

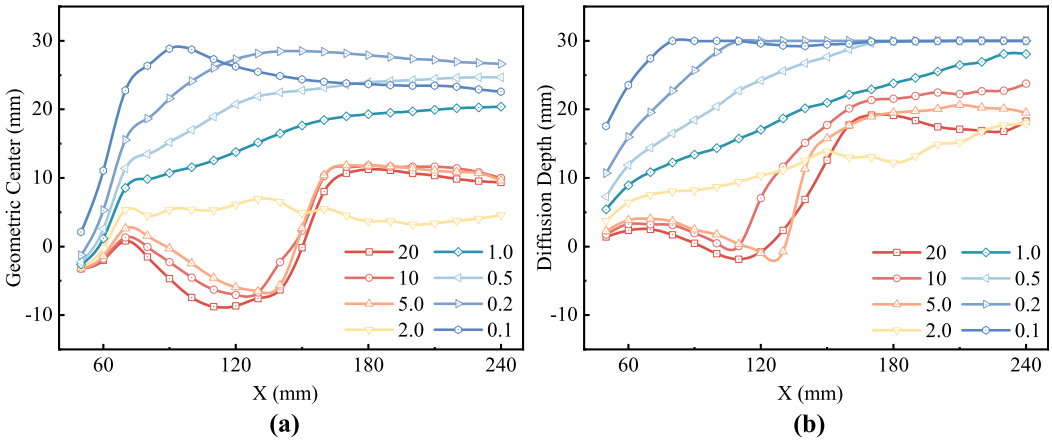

Figure 15. Average value of (**a**) geometric center and (**b**) diffusion depth of particles in the Y-direction along the streamwise direction with different ζ values.

The average value of the particles' geometric center and diffusion depth in the Z-direction along the streamwise direction with different solid-to-gas ratios is shown in Figure 16. Unlike the Y-direction distribution, differences between the geometric center and the diffusion depth in the Z-direction are more pronounced. Only a few particles follow the development of vortex structures reaching deeper into the Z-direction, while most particles still gather along the centerline downstream. Regarding the geometric center of particle distribution, peaks of the particle distribution center appear at different X positions for different cases where particles enter the cavity. These regions with peaks coincide with regions where particles intersect and interact with vortex structures. In contrast, at a ζ of 5.0, since the vortex structures develop along the centerline, the geometric center of particles in the Z-direction remains close to the centerline. The situation is unique for cases where particles do not enter the cavity. The Z-direction diffusion is the deepest between the jet nozzle and the trailing edge of the cavity, under the condition with a ζ of 0.2. However, behind the cavity, in the cases with a ζ of 0.1, the Z-direction diffusion rapidly increases along the streamwise direction and finally reaches the highest level before the outlet. It can be inferred that the reasons are twofold by combining the analysis of vortex structures in Figure 12b. Under lower solid-to-gas ratios, the bow shock and barrel shock enhance the vortex structures' development along the streamwise direction. If particles interact with these structures, they can reach the most significant depth of the vortex regions. As ζ values decrease, the vortex regions are more significant, so particles interacting with vortices will be taken to a greater depth, resulting in deeper diffusion. On the other hand, at a ζ of 0.1, particles quickly reach the top wall and are unaffected by these shock wave structures, resulting in low Z-direction diffusion before the cavity. This low diffusion makes a ζ of 0.1 an exception to the above evolutionary patterns. Behind the cavity, due

to wall reflection effects, particles are forced into the vortex structures, leading to rapid Z-direction diffusion along the development direction of the vortex, showing greater Z-direction diffusion capabilities. Similarly, particles interact well with vortex structures at a ζ of 2.0, also demonstrating greater Z-direction diffusion capabilities.

Regarding the Z-direction diffusion depth, when particles enter the cavity and form effective retention, their diffusion depth can rapidly reach its maximum value. In contrast, when particles do not enter the cavity, their Z-direction diffusion depth develops continuously and slowly along the streamwise direction. Statistics further confirm that at a ζ of 5.0, particles do not form substantial swirling or retention within the cavity. Other trends are similar to those observed for the Z-direction geometric center. When particles do not enter the cavity, the Z-direction diffusion development accelerates as the ζ decreases. However, at a ζ of 0.1, particles quickly enter vortex structures and interact with them, rapidly increasing the particles' Z-direction diffusion depth.

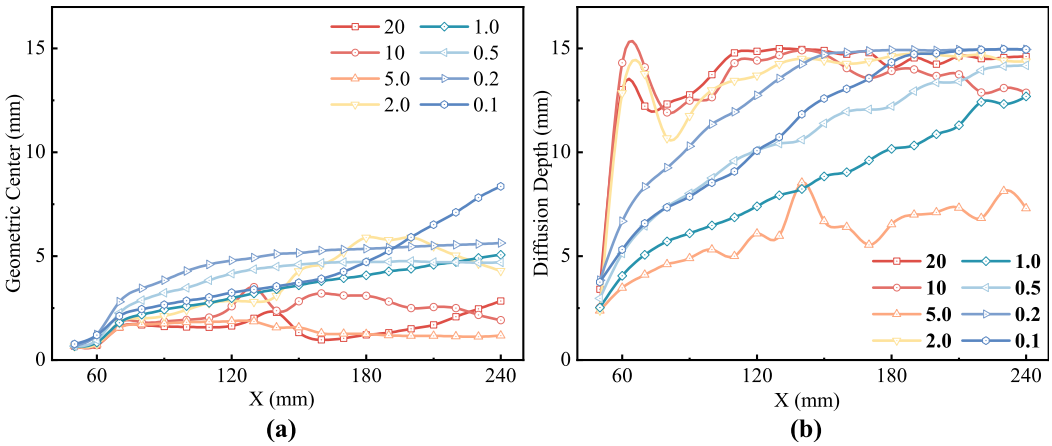

Figure 16. Average value of (**a**) geometric center and (**b**) diffusion depth of particles in the Z-direction along the streamwise direction with different ζ values.

Based on the above analysis, it can be noted that vortex structures are crucial to the movement and diffusion of particles. In this study, flow fields with different solid-to-gas ratios produce varying vortex structures along the streamwise direction, affecting the diffusion of particles. In general, if better diffusion is required, the vortex structures and the particles should be placed in the same regions as much as possible, enhancing the interaction between the particles and the vortex structures.

4.4. Effect on Mixing Efficiency of Powder Fuel

The previous section analyzed and discussed the spatial distribution of particles in the combustion chamber. The spatial distribution of particles reflects the dispersion degree of powder fuel. However, for the combustion organization of powder fuel in ramjets, the relationship between particle concentration and local oxygen concentration is more critical. As the fuel mixing process gained attention, the concept of mixing degree emerged. Researchers have proposed various definitions for different fuel types, focusing on different aspects. There are several definitions of the mixing degree of powder fuel or solid particles in ramjets. In this study, the definition of the particle mixing degree is derived from Chen of the National University of Defense Technology [61]. It is a normalized result related to the flow state parameters of particles and incoming flow and the local concentration of particles and oxygen. The basic formula is as follows:

$$\beta = 1 - \frac{1}{1 + \lg\left[1 + \dfrac{\rho_g v_g Y_{O_2} n_p v_p m_p \eta}{(\rho_g v_g Y_{O_2} - n_p v_p m_p \eta)^2}\right]} \tag{19}$$

Here, β represents the mixing degree of powder fuel. n_p is the local particle concentration (number concentration), and η is the flow ratio of the steady-state oxygen mass flow to the total particle flow. It can be observed from the formula that the mixing degree is a parameter in the range of $[0, 1]$. The mixing degree β approaches 1 only when the ratio of local oxygen content to local particle content is at the set value. An excessively high or excessively low ratio will result in a mixing degree of less than 1. By defining the mixing degrees in this way, the actual mixing effect of powder fuel in this study can be quantitatively evaluated. The average mixing degrees on each slice at 10 mm intervals along the streamwise direction with different solid-to-gas ratio conditions were calculated. The results are shown in Figure 17.

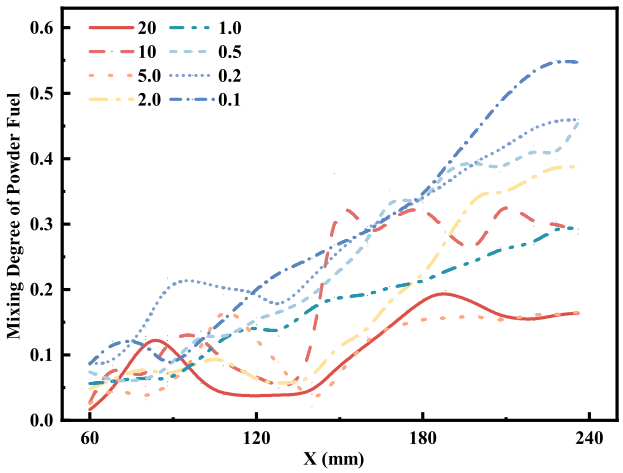

Figure 17. Average mixing degree of powder fuel along the streamwise direction with different ζ values.

Overall, along the streamwise direction, the mixing degree of powder fuel gradually increases, consistent with the particle dispersion. As particles diffuse further downstream, the mixing degree increases. Under conditions of higher solid-to-gas ratios, particles enter the cavity, but statistical results show that entering the cavity does not significantly enhance the mixing degree. Additionally, at the position of X = 130–140 mm, which is the trailing edge of the cavity, the mixing degree of powder fuel reaches its minimum along the flow direction. From the particle distribution analysis, it can be inferred that due to the influence of the wall, particles are more concentrated in this area, causing the powder fuel to deviate significantly from the set concentration ratio.

At ζ = 10, the mixing degree of powder fuel reaches its maximum in the X = 150–170 mm range, while at ζ = 0.1 and ζ = 0.2, it reaches a high level in the X $\geq$ 180 mm range and continues to increase. In this range, as the solid-to-gas ratio changes, the mixing efficiency increases from a minimum of 16% to over 50%, achieving a growth of 30%. In the former case, particles at the cavity's trailing edge appear in the vortex structure's inner region compared to the previous analysis, achieving significant Z-direction diffusion. This phenomenon can also be observed in Figure 16, where the regions with high mixing degrees match the areas where the geometric center significantly develops in the Z-direction in the case of ζ = 10. Similarly, the regions with high mixing degrees for the latter cases match the areas where their particle distribution geometric centers significantly develop in the Z-direction. However, the causes of this phenomenon for ζ = 0.1 and ζ = 0.2 are not consistent. According to Figure 12b, the case of ζ = 0.1 is due to particles being directly acted upon by the upper wall, forcing them into the vortex core, leading to rapid diffusion as they follow the vortex rotation. The case of ζ = 0.2 results from the combined effects of the wall and vortex structure boundary, causing particles to continuously develop in

the Z-direction until reaching a high level. From the previous analysis, the primary spatial distribution factor affecting the enhancement of the mixing degree of powder fuel is the Z-direction distribution of particles. The main factor influencing the Z-direction distribution of particles should be the rotating region within the vortex structure. More effective mixing enhancement should revolve around large-scale vortices rather than improving turbulence or small-scale vortices.

This section quantitatively analyzed the mixing degree of powder fuel, evaluated the differences in mixing degree distribution under different solid-to-gas ratio conditions, and analyzed the factors affecting the distribution of particle mixing degree based on the previous analysis. It confirmed the earlier conclusion that the enhancement of powder fuel mixing is more related to the rotating regions around large-scale vortices. More effective mixing enhancement can be achieved by adjusting the solid-to-gas ratio to interact with vortex structures, as in the case of $\zeta = 10$ in this study, or by enhancing the influence of vortex structures and inducing particles into the vortex interior for higher mixing levels.

5. Conclusions

Based on the Euler–Lagrangian methods, this study conducted a series of numerical simulations on supersonic gas-solid two-phase flows in the combustion chamber with strong shear and discontinuity. After verifying the reliability of the two-phase flow solution methods, the flow processes and mixing characteristics under transverse jets with varying solid-to-gas ratios from 20 to 0.1 in supersonic flow were discussed. The shock wave structures, vortex structure evolutionary patterns, particle diffusion patterns, powder fuel mixing degree, and their internal correlations with different solid-to-gas ratios were analyzed in detail. The main conclusions were as follows:

1. The solid-to-gas ratio plays a critical role in the behavior of shock waves in the supersonic combustion chamber. When the solid-to-gas ratio exceeds 1.0, the induced shock waves from the top wall dominate. As the solid-to-gas ratio decreases, the intensity and position of the λ shock waves, bow shock waves, and cylindrical shock waves change, leading to complex shock wave interactions. These changes result in variations in shock wave structures, affecting the development of the shear layer and the main flow process.
2. The solid-to-gas ratio significantly affects the vortex structures and their development in the supersonic combustion chamber. Triangular recirculation vortices appear in the cavity's front part at higher solid-to-gas ratios due to sudden expansion. As the solid-to-gas ratio increases, these recirculation vortices extend along the flow direction, gradually expanding to cover the entire cavity. Additionally, in regions with significant shock wave interactions, the turbulent kinetic energy levels of the flow field increase, enhancing flow instability.
3. Particle diffusion shows significant differences at varying solid-to-gas ratios. At higher ratios, particles enter the cavity following the stream and are retained in the cavity. As the ratio decreases, particles pass through the cavity or are deflected back into the flow field, continuing downstream with increased Z-direction diffusion. At very low ratios (e.g., 0.1), particles enter the vortex structures due to wall effects, leading to rapid Z-direction diffusion. Vortex structures are crucial for particle movement and diffusion. Different solid-to-gas ratios produce varying vortex structures, altering particle diffusion. For better diffusion, vortex structures and particles should be in the same regions to enhance interaction.
4. The development distribution of powder fuel mixing degrees shows certain differences at different solid-to-gas ratios. At certain specific ratios, the mixing degree of the fuel reaches a high level within a specific range. The interaction between powder

fuels and the peripheral rotating regions of these vortices significantly improves the mixing efficiency, with the highest average mixing efficiency increased by 30%. Overall, the enhancement of powder fuel mixing is more related to the rotating regions around large-scale vortices. Higher mixing degrees can be achieved by adjusting the appropriate solid-to-gas ratio to interact with vortex structures or by enhancing the influence of vortex structures and inducing particles into the vortices.

Author Contributions: Software, M.J. and K.M.; validation, Z.L., M.J. and W.W.; formal analysis, Z.L. and M.J.; investigation, Z.L.; data curation, Z.L., G.X. and Y.M.; writing—original draft, Z.L.; writing—review & editing, Z.L., M.J., S.H., K.M. and H.L.; funding acquisition, M.J. and K.M. All authors have read and agreed to the published version of the manuscript.

Funding: This research was funded by the National Natural Science Foundation of China (12302336).

Data Availability Statement: Data will be made available on request.

Conflicts of Interest: The authors declare no conflict of interest.

Abbreviations

The following abbreviations are used in this manuscript:

a	Gaussian distribution width control parameter
A_p	Surface area of particle
β	Mixing degree of powder fuel
C_D	Drag coefficient of particle
c_p	Heat capacity of particle
D_{ij}	Binary mass diffusion coefficient of species i in species j
d_{ij}	Deformation tensor
$D_{i,m}$	Mass diffusion coefficient for species i (gas)
$\mathrm{d_p}$	Particle diameter of powder fuel
$D_{T,i}$	Thermal diffusion coefficient for species i (gas)
ϵ_p	Particle emissivity
η	Mass flow ratio of oxygen and particle entering the system
$\vec{F}_d$	Drag force of particle
$\vec{F}$	Additional force added to particle
$\vec{F}_{\text{pressure gradient}}$	Pressure gradient force of particle
$\vec{F}_{\text{Saffman's lift force}}$	Saffman's lift force of particle
Γ_k	Effective diffusivity for k
Γ_ω	Effective diffusivity for ω
G_k	Generation of k
G_ω	Generation of ω
h	Convective heat transfer coefficient
$\vec{J}_i$	Diffusion flux of species i (gas)
k	Turbulence kinetic energy
K	Constant for Saffman's lift force
k_{eff}	Effective conductivity of gas
k_m	Molecular conductivity of gas
k_t	Turbulent thermal conductivity
Ma	Mach number
MAPE	Mean absolute percentage error
$\dot{\mathrm{m}}_\mathrm{g}$	Mass flow rate of jet
$\dot{\mathrm{m}}_\mathrm{p}$	Mass flow rate of powder fuel
$\mathrm{m_p}$	Particle mass of powder fuel
μ_{eff}	Effective dynamic viscosity of gas
μ	Molecular viscosity of gas

μ_t	Turbulent viscosity
$N_{\text{in parcel}}$	Number of particles in parcel
n_p	Number concentration of particles
ν	Kinematic viscosity
ω	Specific dissipation rate
P_0	Total pressure of supersonic inflow
p_g	Static pressure of gas
ϕ_p	Particle variable
$\overline{\phi}_{\text{node}}$	Accumulation of particle variable on node
R^2	Coefficient of determination
Re_p	Relative Reynolds number of particle
ρ_g	Density of gas
ρ_{p}	Density of powder fuel
R_i	Net rate of production of species i (gas)
Sc_t	Turbulent Schmidt number
S_h	Energy source term added to continuous phase from dispersed phase
S_i	Net rate of production of species i (gas) from dispersed phase
σ	Stefan–Boltzmann constant
S_k	Source terms of k from dispersed phase
S_m	Mass source term added to continuous phase from dispersed phase
S_ω	Source terms of ω from dispersed phase
SST $k-\omega$ model	Shear-Stress Transport $k-\omega$ turbulence model
S_u	Momentum source term added to continuous phase from dispersed phase
T_0	Total temperature of supersonic inflow
$\overline{\overline{\tau}}$	Stress tensor of gas
T_g	Static temperature of gas
Θ_R	Radiation temperature
T_{p}	Static temperature of powder fuel
$\vec{v}_g$ or v_g	Velocity of gas
$\vec{v}_i$	Velocity of species i (gas)
$\vec{v}_p$ or v_p	Velocity of powder fuel
w	Weighting function
Δx	Characteristic length scale of cell
X_i	Mole fraction of species i (gas)
$\vec{x}_p^n$	Position of particle
$\vec{x}_{\text{node}}$	Position of node
y^+	Dimensionless wall distance
Y_i	Mass fraction of species i (gas)
Y_k	Dissipation of k
Y_ω	Dissipation of ω
$\mathrm{Y}_{\mathrm{O}_2}$	Mass fraction of O_2
ζ	Solid-to-gas ratio of injection

References

1. Fry, R.S. A century of ramjet propulsion technology evolution. *J. Propuls. Power* **2004**, *20*, 27–58. [CrossRef]
2. Spalding, D.B. *Some Fundamentals of Combustion*; Butterworths: London, UK, 1955.
3. Dugger, G.L. Recent advances in ramjet combustion. *ARS J.* **1959**, *29*, 819–827. [CrossRef]
4. Branstetter, J.R.; Lord, A.M.; Gerstein, M. *Combustion Properties of Aluminum as Ram-Jet Fuel*; Technical Report E51B02; NACA Research Memorandum: Washington, DC, USA 1951.
5. Olson, W.T.; Gibbons, L.C. *Status of Combustion Research on High-Energy Fuels for Ram Jets*; Technical Report E51D23; NACA Research Memorandum: Washington, DC, USA, 1951.
6. Goroshin, S.; Higgins, A.; Kamel, M. Powdered metals as fuel for hypersonic ramjets. In Proceedings of the 37th Joint Propulsion Conference and Exhibit, Salt Lake City, UT, USA, 8–11 July 2001; p. 3919.

7. Jung, W.; Baek, S.; Park, J.; Kwon, S. Combustion characteristics of ramjet fuel grains with boron and aluminum additives. *J. Propuls. Power* **2018**, *34*, 1070–1079. [CrossRef]
8. Miller, T.; Herr, J. Green rocket propulsion by reaction of Al and Mg powders and water. In Proceedings of the 40th AIAA/ASME/SAE/ASEE Joint Propulsion Conference and Exhibit, Fort Lauderdale, FL, USA, 11–14 July 2004; p. 4037.
9. Gany, A. Effect of fuel properties on the specific thrust of a ramjet engine. *Def. Sci. J. New Delhi* **2006**, *56*, 321. [CrossRef]
10. Young, G.; Balar, R.; Yu, K. Combustor Experiments of Reacting Nano-Particle Laden Flows. In Proceedings of the 42nd AIAA/ASME/SAE/ASEE Joint Propulsion Conference & Exhibit, Sacramento, CA, USA, 9–12 July 2006; p. 4401.
11. Athawale, B.; Asthana, S.; Singh, H. Burning rate studies of metal powder (Ti, Ni)–based fuel-rich propellants. *J. Energetic Mater.* **2004**, *22*, 55–68. [CrossRef]
12. Rosenband, V.; Gany, A. Ignition characteristics of nanosize zirconium and titanium Powders. In Proceedings of the 42nd AIAA/ASME/SAE/ASEE Joint Propulsion Conference & Exhibit, Sacramento, CA, USA, 9–12 July 2006; p. 4406.
13. Shen, H.; Xia, Z.; Hu, J. Theoretical performance analysis of the powdered fuel ramjet. *J. Propuls. Technol. Beijing* **2007**, *28*, 181.
14. Hu, J.; Xia, Z.; Shen, H.; Kong, L.; Huang, L. Experimental investigation on powdered fuel ramjet combustion performance. *Trans. Jpn. Soc. Aeronaut. Space Sci.* **2013**, *56*, 337–342. [CrossRef]
15. Shen, H.; Xia, Z.; Hu, J.; Jin, J. Experimental investigation on self-sustaining combustion of powdered metal fuel ramjet. *J. Solid Rocket Technol.* **2009**, *32*, 145–149.
16. Li, C.; Hu, C.; Zhu, X.; Hu, J.; Li, Y.; Hu, X. Experimental study on the thrust modulation performance of powdered magnesium and CO_2 bipropellant engine. *Acta Astronaut.* **2018**, *147*, 403–411. [CrossRef]
17. Li, C.; Hu, C.; Xin, X.; Li, Y.; Sun, H. Experimental study on the operation characteristics of aluminum powder fueled ramjet. *Acta Astronaut.* **2016**, *129*, 74–81. [CrossRef]
18. Hu, X.; Xu, Y.; Ao, W.; Zeng, Z.; Hu, C.; Zhu, X. Ignition model of boron particle based on the change of oxide layer structure. *Proc. Combust. Inst.* **2019**, *37*, 3033–3044. [CrossRef]
19. Liu, D.; Xia, Z.; Huang, L.; Hu, J. Boron particle combustion in solid rocket ramjets. *J. Aerosp. Eng.* **2015**, *28*, 04014112. [CrossRef]
20. Williams, O.J.; Nguyen, T.; Schreyer, A.M.; Smits, A.J. Particle response analysis for particle image velocimetry in supersonic flows. *Phys. Fluids* **2015**, *27*, 7. [CrossRef]
21. Huang, W.; Du, Z.b.; Yan, L.; Xia, Z.x. Supersonic mixing in airbreathing propulsion systems for hypersonic flights. *Prog. Aerosp. Sci.* **2019**, *109*, 100545. [CrossRef]
22. Sun, M.; Wang, H.; Cai, Z.; Zhu, J. *Unsteady Supersonic Combustion*; Springer Nature Singapore Pte Ltd.: Singapore, 2020.
23. Ben-Yakar, A.; Mungal, M.; Hanson, R. Time evolution and mixing characteristics of hydrogen and ethylene transverse jets in supersonic crossflows. *Phys. Fluids* **2006**, *18*, 2. [CrossRef]
24. Mai, T.; Sakimitsu, Y.; Nakamura, H.; Ogami, Y.; Kudo, T.; Kobayashi, H. Effect of the incident shock wave interacting with transversal jet flow on the mixing and combustion. *Proc. Combust. Inst.* **2011**, *33*, 2335–2342. [CrossRef]
25. Rana, Z.A.; Thornber, B.; Drikakis, D. Transverse jet injection into a supersonic turbulent cross-flow. *Phys. Fluids* **2011**, *23*, 4. [CrossRef]
26. Sun, M.; Hu, Z. Formation of surface trailing counter-rotating vortex pairs downstream of a sonic jet in a supersonic cross-flow. *J. Fluid Mech.* **2018**, *850*, 551–583. [CrossRef]
27. Sun, M.B.; Hu, Z.W. Mixing in nearwall regions downstream of a sonic jet in a supersonic crossflow at Mach 2.7. *Phys. Fluids* **2018**, *30*, 10. [CrossRef]
28. Techer, A.; Moule, Y.; Lehnasch, G.; Mura, A. Mixing of fuel jet in supersonic crossflow: Estimation of subgrid-scale scalar fluctuations. *AIAA J.* **2018**, *56*, 465–481. [CrossRef]
29. Sun, M.B.; Hu, Z. Generation of upper trailing counter-rotating vortices of a sonic jet in a supersonic crossflow. *AIAA J.* **2018**, *56*, 1047–1059. [CrossRef]
30. Liang, C.H.; Sun, M.B.; Liu, Y.; Yang, Y.X. Shock wave structures in the wake of sonic transverse jet into a supersonic crossflow. *Acta Astronaut.* **2018**, *148*, 12–21. [CrossRef]
31. Huang, W.; Wang, Z.g.; Wu, J.p.; Li, S.b. Numerical prediction on the interaction between the incident shock wave and the transverse slot injection in supersonic flows. *Aerosp. Sci. Technol.* **2013**, *28*, 91–99. [CrossRef]
32. Gerdroodbary, M.B.; Ganji, D.; Amini, Y. Numerical study of shock wave interaction on transverse jets through multiport injector arrays in supersonic crossflow. *Acta Astronaut.* **2015**, *115*, 422–433. [CrossRef]
33. Ukai, T.; Zare-Behtash, H.; Erdem, E.; Lo, K.H.; Kontis, K.; Obayashi, S. Effectiveness of jet location on mixing characteristics inside a cavity in supersonic flow. *Exp. Therm. Fluid Sci.* **2014**, *52*, 59–67. [CrossRef]
34. Ukai, T.; Zare-Behtash, H.; Lo, K.H.; Kontis, K.; Obayashi, S. Effects of dual jets distance on mixing characteristics and flow path within a cavity in supersonic crossflow. *Int. J. Heat Fluid Flow* **2014**, *50*, 254–262. [CrossRef]
35. Roos, T.; Pudsey, A.; Bricalli, M.; Ogawa, H. Numerical investigation of fuel mixing with upstream crescent cavities in a scramjet combustor. *Acta Astronaut.* **2020**, *177*, 611–626. [CrossRef]

36. Gruber, M.; Baurle, R.; Mathur, T.; Hsu, K.Y. Fundamental studies of cavity-based flameholder concepts for supersonic combustors. *J. Propuls. Power* **2001**, *17*, 146–153. [CrossRef]
37. Yang, Y.; Wang, Z.; Zhang, Y.; Sun, M.; Wang, H. Flame stabilization with a rear-wall-expansion cavity in a supersonic combustor. *Acta Astronaut.* **2018**, *152*, 752–756. [CrossRef]
38. Ding, H.; Zhuo, C.; Deng, H.; Chen, X.; Sun, B. Numerical investigate on flow process and mixing characteristics of hydrogen/aluminum powder two-phase fuel under different inlet and injection conditions. *Int. J. Hydrogen Energy* **2024**, *53*, 1170–1189. [CrossRef]
39. Ding, H.; Zhuo, C.; Deng, H.; Hu, W.; Chen, X. Numerical study on coupled flow characteristics of a gas-solid two-phase jet in a supersonic crossflow. *Int. J. Multiph. Flow* **2023**, *168*, 104583. [CrossRef]
40. Ding, H.m.; Zhuo, C.f.; Chen, X.; Deng, H.y. Numerical study on powder fuel injection characteristics of powder fuel scramjet. *Powder Technol.* **2022**, *399*, 117169. [CrossRef]
41. Feng, Y.; Luo, S.; Song, J.; Xia, K.; Xu, D. Numerical investigation on the combustion characteristics of aluminum powder fuel in a supersonic cavity-based combustor. *Appl. Therm. Eng.* **2023**, *221*, 119842. [CrossRef]
42. Feng, Y.; Luo, S.; Song, J.; Xu, D. Numerical investigation on the combustion characteristics of powder fuel under different regulation parameters. *Aerosp. Sci. Technol.* **2023**, *142*, 108608. [CrossRef]
43. Feng, Y.; Luo, S.; Song, J.; Xu, D. Numerical investigation on flow and mixing characteristics of powder fuel under strong shear and shock wave interaction. *Energy* **2023**, *263*, 126061. [CrossRef]
44. Yang, J.; Hu, C.; Qiang, W.; Hu, J.; Hu, X.; Zhu, X. Experimental investigation on the starting and flow regulation characteristics of powder supply system for powder engines. *Acta Astronaut.* **2021**, *180*, 73–84. [CrossRef]
45. Batchelor, G.K. *An Introduction to Fluid Dynamics*; Cambridge University Press: Cambridge, UK, 2000.
46. Kee, R.J.; Coltrin, M.E.; Glarborg, P. *Chemically Reacting Flow: Theory and Practice*; John Wiley & Sons, Inc.: Hoboken, NJ, USA, 2005.
47. Meneveau, C.; Poinsot, T. Stretching and quenching of flamelets in premixed turbulent combustion. *Combust. Flame* **1991**, *86*, 311–332. [CrossRef]
48. Menter, F.R. Two-equation eddy-viscosity turbulence models for engineering applications. *AIAA J.* **1994**, *32*, 1598–1605. [CrossRef]
49. Liu, B.; Zhang, X.; Wang, L.; Hong, H. Fluidization of non-spherical particles: Sphericity, Zingg factor and other fluidization parameters. *Particuology* **2008**, *6*, 125–129. [CrossRef]
50. Sun, D.; Liu, P.; Hui, S.; Yan, T.; Song, N. Experimental Study on the Mass Flow Rate Characteristics of a Fluidized Bed Powder Fuel Feeding System. *Powder Technol.* **2025**, *449*, 120351. [CrossRef]
51. Li, A.; Ahmadi, G. Dispersion and deposition of spherical particles from point sources in a turbulent channel flow. *Aerosol Sci. Technol.* **1992**, *16*, 209–226. [CrossRef]
52. Saffman, P.G. The lift on a small sphere in a slow shear flow. *J. Fluid Mech.* **1965**, *22*, 385–400. [CrossRef]
53. Kaufmann, A.; Moreau, M.; Simonin, O.; Helie, J. Comparison between Lagrangian and mesoscopic Eulerian modelling approaches for inertial particles suspended in decaying isotropic turbulence. *J. Comput. Phys.* **2008**, *227*, 6448–6472. [CrossRef]
54. Apte, S.; Gorokhovski, M.; Moin, P. LES of atomizing spray with stochastic modeling of secondary breakup. *Int. J. Multiph. Flow* **2003**, *29*, 1503–1522. [CrossRef]
55. Liou, M.S. A sequel to ausm: Ausm+. *J. Comput. Phys.* **1996**, *129*, 364–382. [CrossRef]
56. Anderson, W.K.; Bonhaus, D.L. An implicit upwind algorithm for computing turbulent flows on unstructured grids. *Comput. Fluids* **1994**, *23*, 1–21. [CrossRef]
57. Spaid, F.W.; Zukoski, E. A study of the interaction of gaseous jets from transverse slots with supersonic external flows. *AIAA J.* **1968**, *6*, 205–212. [CrossRef]
58. Sriram, A.; Mathew, J. Improved prediction of plane transverse jets in supersonic crossflows. *AIAA J.* **2006**, *44*, 405–408. [CrossRef]
59. Sommerfeld, M. The structure of particle-laden, underexpanded free jets. *Shock Waves* **1994**, *3*, 299–311. [CrossRef]
60. Quirk, J.J. *A Contribution to the Great Riemann Solver Debate*; Springer: Berlin/Heidelberg, Germany, 1997.
61. Chen, B.; Xia, Z.; Wang, D.; Hu, J.; Ma, L.; Zhao, X. Study on mixing process assessment method in solid ramjet. *J. Solid Rocket Technol.* **2013**, *36*, 731–735.